

**UNCLASSIFIED**

---

**AD 296 263**

---

*Reproduced  
by the*

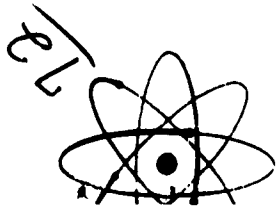
**ARMED SERVICES TECHNICAL INFORMATION AGENCY  
ARLINGTON HALL STATION  
ARLINGTON 12, VIRGINIA**



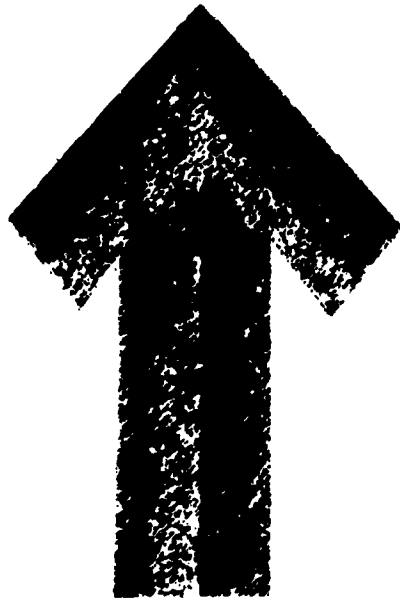
---

**UNCLASSIFIED**

NOTICE: When government or other drawings, specifications or other data are used for any purpose other than in connection with a definitely related government procurement operation, the U. S. Government thereby incurs no responsibility, nor any obligation whatsoever; and the fact that the Government may have formulated, furnished, or in any way supplied the said drawings, specifications, or other data is not to be regarded by implication or otherwise as in any manner licensing the holder or any other person or corporation, or conveying any rights or permission to manufacture, use or sell any patented invention that may in any way be related thereto.

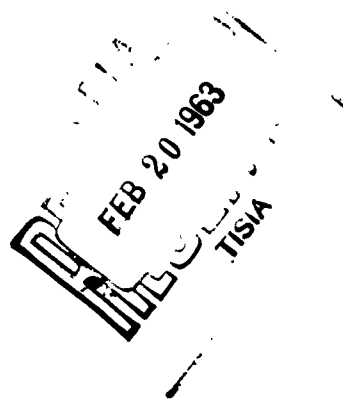
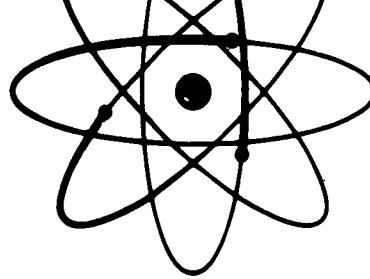


AD No. **296 263**  
ISTIA FILE COPY



**296 263**

*NP-12194*  
Report Number



**NO OTS**

United States Atomic Energy Commission  
*Division of Technical Information*



## CONTENTS

April 20, 1962

Semiannual Technical Report No. 2

# VELA-UNIFORM DYNAMIC PROPERTIES OF ROCKS

Prepared for:

ELECTRONIC SYSTEMS DIVISION  
AIR FORCE SYSTEMS COMMAND  
LAURENCE G. HANSCOM FIELD  
BEDFORD, MASSACHUSETTS

By V. G. Gregson D. R. Grine  
Poulter Laboratories

SRI Project No. PC-11-36-0

ARPA Order Number: 180-61 Amendment 2) and 292-62  
Project Code Numbers: 8100 Task 2) and 8652  
Date of Contract: 1 March 1961  
Name of Contractor: Stanford Research Institute  
Amount of Contract: \$220,400  
Contract Number: AF 19(604)-8419  
Contract Expiration Date: 15 August 1963  
Project Scientist: G. R. Fowler  
Phone Number: Davenport 6-6200, Ext. 3138

Approved:

*G. R. Fowler*  
G. R. FOWLER  
PROJECT SUPERVISOR

Copy No. 50

iii

## LIST OF ILLUSTRATIONS LIST OF TABLES

I INTRODUCTION AND SUMMARY	1
II EXPERIMENTAL METHODS	1
A Pellet Method	1
B Beveled Pellet Method	12
C Plane-Wave Wedge Method	21
D Two-Dimensional Wedge Experiment	24
III RESULTS	27
A Quartz	27
B Quartz Rocks	27
C Calcite	42
D Carbonate Rocks	46
APPENDIX A PYTHAGORIC DESCRIPTIONS	55
APPENDIX B SAMPLE TESTING AND PREPARATION	69
APPENDIX C PROGRAM FOR TWO-DIMENSIONAL WEDGE EXPERIMENTS	75
APPENDIX D RELATIONSHIPS OF ROCK PARAMETERS	109
REFERENCES	117

# ILLUSTRATIONS

Fig. 1 Hugoniot Equation of State of a Solid in the Vicinity of the Yield Point . . . . .	7
Fig. 2 Diagram of Experimental Setup . . . . .	10
Fig. 3 Diagram of Experimental Assembly . . . . .	10
Fig. 4 Simplified Diagram of the Assembly Undergoing Shock Loading . . . . .	11
Fig. 5 Streak Camera Photograph for a Z-cut Calcite Crystal . . . . .	13
Fig. 6 Diagram of the Streak Camera Photograph . . . . .	15
Fig. 7 Correspondence of Times and Distances at Shot to Distances on Streak Record . . . . .	15
Fig. 8 Schematic of Revealed Pellet Experiment . . . . .	16
Fig. 9 Revealed Pellet Record - Sandstone (Shot No. 7861) . . . . .	16
Fig. 10 Graphical Interpretation of Revealed Pellet Record (Shot No. 7861) . . . . .	19
Fig. 11 Schematic of Plane-Wave Wedge Experiment . . . . .	21
Fig. 12 Plane-Wave Wedge Record of Sigma Quartzite . . . . .	22
Fig. 13 Graphical Interpretation of Plane-Wave Wedge Experiment . . . . .	23
Fig. 14 Side View of Two Dimensional Wedge Experiment . . . . .	25
Fig. 15 Schematic of Two Mirror Wedge Experiment . . . . .	26
Fig. 16 Stream vs Particle Velocity for Quartz . . . . .	31
Fig. 17 Stream vs Particle Velocity for Quartz . . . . .	32
Fig. 18 Hugoniot for Quartz and Quartz Rocks . . . . .	37
Fig. 19 Stream vs Particle Velocity for Quartz Rocks . . . . .	38
Fig. 20 Average First Wave Velocity vs Porosity for Quartz and Carbonate Rocks . . . . .	40
Fig. 21 Peak Stream of First Wave vs Porosity for Quartz and Carbonate Rocks . . . . .	41
Fig. 22 Stream vs Particle Velocity for Calcite and Carbonate Rocks . . . . .	42
Fig. 23 Stream vs Particle Velocity for Calcite and Carbonate Rocks . . . . .	43
Fig. 24 Hugoniot for Calcite and Carbonate Rocks . . . . .	44
Fig. 25 Hugoniot for Carbonate Rocks . . . . .	52
Fig. 26 X-Ray Diffraction Pattern of Arkansas Novaculite . . . . .	58
Fig. 27 Fabric Orientation of Cocaine Sandstone . . . . .	60
Fig. 28 Classification of Pure Sandstones . . . . .	61

# ILLUSTRATIONS

Fig. 29 Fabric Orientation of Kurena Quartzite . . . . .	61
Fig. 30 Fabric Orientation of Spargen Limestone. . . . .	65
Fig. 31 Classification of Calcarenites . . . . .	66
Fig. 32 Fabric Orientation of Yale Marble. . . . .	68
Fig. 33 Coordinate Systems Used in Hexagonal Crystals. . . . .	74
Fig. 34 Plot of Heads $1\sigma$ of Cubic and Quadratic Polynomials. . . . .	75
Fig. 35 Observed and Predicted Distribution of Longest Runs. . . . .	80
Fig. 36 Shear Record Velocity $10, \sigma_{\text{eff}}$ . . . . .	81
Fig. 37 Shock Velocity $G_{\text{max}}$ . . . . .	82
Fig. 38 Particle Velocity Geometry . . . . .	84
Fig. 39 Impedance Match Diagram. . . . .	85
Fig. 40 Stream Profiles at Selected Times $\Delta T < \tau$ . . . . .	89
Fig. 41 Stream Particle Velocity Diagram, $\Delta T < \tau$ . . . . .	90
Fig. 42 Time Position Diagram, $\Delta T < \tau$ . . . . .	91
Fig. 43 SC as Profiles at Selected Times, $\Delta T > \tau$ . . . . .	93
Fig. 44 Stream Particle Velocity Diagram, $\Delta T > \tau$ . . . . .	94
Fig. 45 Time Position Diagram, $\Delta T > \tau$ . . . . .	94
Fig. 46 Flow Chart . . . . .	97

# TABLES

Table I Summary of Zip Moments . . . . .	28
Table II Summary of Rock Information. . . . .	29
Table III Summary of Experimental Data for Quartz and Calcite . . . . .	30
Table IV Summary of Data for Quartz Rocks, Two-Dimensional Ridge Experiments. . . . .	31
Table V Summary of Data for Carbonate Rocks, Two-Dimensional Ridge Experiments. . . . .	45
Table VI Summary of Data for Plane-Wave Shocks . . . . .	51

## I INTRODUCTION AND SUMMARY

Much interest and study is currently directed toward the dynamic properties of rocks. This interest is primarily the result of problems arising in the detection of nuclear explosions. Specifically, the pressure behavior of rocks controls the frequency spectrum and the amplitude of the resulting seismic signals from an explosion. The energy of a seismic signal is small compared to the energy of the explosion. The difference in energy between the explosion and the seismic signal is accounted for in the region near the explosion. The energy is left behind by the shock wave and exists as heat, increased surface area, and material flow.

At very high pressures any anisotropy of stress from material strength is conventionally neglected in comparison to the mean stress. The material is assumed fluid and hydrodynamic theory is applied. Propagation in this region is nonlinear. Energy from the shock is left in the medium as heat, surface energy, etc. This changes the shape of the shock wave as it travels. The material properties which influence shock propagation are the Rankine-Hugoniot curve and the adiabatic pressure-volume curves.

As the pressure of the shock from the explosion decays, there is a radius beyond which the effects due to material strength can no longer be neglected. The shock front becomes unstable and breaks into two shock fronts, and this two-wave structure complicates the description and prediction of shock propagation in this intermediate region. Moreover, knowledge of more material properties is required for accurate predictions. The yield behavior under uniaxial, high strain-rate loading must be known in order to determine the maximum amplitude of elastic waves and to determine the pressure range within which a double shock wave occurs.

The shock wave will continue to decay until, at some radius, the strains are completely elastic. Studies in energy coupling of underground nuclear explosions show that it is important to be able to predict the radius and the critical maximum amplitude beyond which the subsequent propagation can be considered elastic. In the theory of coupling, which has been partially verified experimentally, these two quantities enter

directly and, in fact, constitute the major unknowns in computing the amplitude of seismic waves at large distances from an explosion.

The goal of the present program is to measure some of the material properties under shock conditions in simple rocks and minerals. The pressure region of interest is the region in which the material strength of the rock affects the shock wave. The property that is measured is the Hugoniot equation of state. From measurements of this function, information is obtained about such aspects as phase transitions, elastic wave amplitudes and velocities, and pressure-volume relations above the elastic limit. The measurements in the program also permit a comparison of the behavior of single crystals with the polycrystalline rock.

The rock properties at these pressures are correlated insofar as possible with the properties that can be measured in their initial state. The initial state properties are porosity, grain size, preferential mineral alignment, and degree of cementation.

The minerals studied are quartz and calcite in both crystal and polycrystalline form. The polycrystalline rocks of quartz and calcite each include one porous and one non-porous rock.

Two-dimensional wedge experiments supply most of the data; plane-wave measurements provide checks at the lower pressures and give some values at higher pressures. Experiments were completed on:

Arkansas novaculite	30 to 200 kilobars
Sioux quartzite	10 to 230 kilobars
Eschscholtz quartzite	15 to 60 kilobars
Concannon sandstone	2 to 130 kilobars
Yule marble	10 to 250 kilobars
Spergen limestone	1 to 200 kilobars
Quartz	230 kilobars
Calcite	20 to 130 kilobars

In summary, the results indicate the following:

1. A two-wave front in the shock wave is recorded in each material. This is thought to be the result of failure at the elastic limit by either fracture or slip. A three-wave structure is sometimes recorded in the carbonates. The additional front is probably due to a phase transition.
2. There is a difference between the Hugoniot of single crystals and polycrystalline rocks. Compared to the single crystals, there is a

decrease in peak stress and velocity in the first wave of the polycrystalline rocks. This is greatest for the porous rocks and least for polycrystalline rocks with no porosity. The peak stress and velocity of the first wave depends strongly on porosity but it has not been demonstrated which parameters controlling porosity (e.g., cementation, grain size, sorting, etc.) are most important.



## II EXPERIMENTAL METHODS

Parts of the following pages are quoted from the Semiannual Technical Report of October 20, 1961.

The principles of experimental methods for determining Hugoniot equations of state, utilizing explosively induced shock waves, have been reviewed in detail by Rice, *et al.* These methods are based on the Rankine Hugoniot jump conditions expressing conservation of mass, momentum, and energy across a shock front. These may be written:

$$\frac{V_1}{V_0} = 1 - \frac{u_1 - u_0}{U_1 - u_0} \quad (\text{mass})$$

$$\sigma_1 - \sigma_0 = \rho_0 (U_1 - u_0)(u_1 - u_0) \quad (\text{momentum}) \quad (1)$$

$$E_1 - E_0 = \frac{(\sigma_1 + \sigma_0)}{2} (V_0 - V_1) \quad (\text{energy})$$

where  $V(=1/\rho)$  is specific volume,  $u$  is mass velocity,  $U$  is shock velocity,  $\sigma$  is compressive stress normal to the shock front, and  $E$  is specific internal energy. All wave and particle velocities used in this report refer to laboratory coordinates. Subscripts "0" refer to the state ahead of the shock front, and subscripts "1" to the state immediately behind the front.

Considering the initial state known, there remain five unknown quantities and three relations. Hence, measurement of any two allows the remaining quantities to be computed. In the experiments to be described both the shock wave velocity and the free-surface velocity produced upon reflection of the shock from a free boundary are measured. These, together with a relation between free-surface velocity and particle velocity prior to reflection, are sufficient to determine the stress-density-energy state behind the shock front. A series of measurements with different shock intensities thus determine the Hugoniot equation of state, or locus of states attainable through a single shock transition.

The particle velocity prior to reflection is, to an adequate approximation, one half the free-surface velocity. This approximation is based on the condition that entropy changes are small;<sup>2</sup> it works well for metals, crystals, and rocks with no porosity. It does not work past the elastic limit in the porous rocks, because the work expended in closing the pore space is largely irreversible and thus involves large entropy changes. In that case a more devious procedure is required to establish the particle velocity. It will be described in Section III.

It should be noted that while this procedure establishes the Hugoniot equation of state, no experimental information concerning the components of stress parallel to the shock front is obtained. These lateral stresses are related to the observed stress, normal to the front, through the effective Poisson's ratio, and must exist to maintain the macroscopic strain uniaxial as is required by symmetry. In isotropic materials the net strain is normal to the shock front; in anisotropic materials it may be inclined to the front but is still uniaxial.

It can be generally stated that, in any given solid, a range of final shock stresses exists for which a single shock front is unstable. This is due to violation of the sufficient condition for shock stability<sup>1</sup>

$$\frac{\partial^2 \sigma}{\partial v^2} \geq 0 \quad (2)$$

where  $\sigma$ , is the component of stress normal to the shock front. It is easily shown that this condition is violated in a solid for stresses in the vicinity of the yield stress appropriate to the case of one-dimensional strain. (It may also be violated elsewhere if phase transitions occur.) Thus, for a range of shock stresses, a single front breaks up into a double front. The first of these travels with elastic velocity (dilatational velocity in isotropic materials) and has a stress amplitude such that the difference between the principal stresses behind the front is just equal to the yield strength. The stress amplitude of this wave in the direction normal to the wave front is termed the Hugoniot elastic limit.

This elastic forerunner is followed by a slower shock front in which the effective rigidity modulus is reduced (or even zero) and which carries the material to the final state. The velocity of the second front increases with stress and for sufficiently high stresses this front will

overtake the elastic front under these conditions a single front is again stable.

The above relationships are depicted qualitatively in Fig. 1. In this diagram the Hugoniot equation of state is represented by the curve ABCD. Point B is the Hugoniot elastic limit and is the amplitude of the first wave when a double wave exists from Eq. (1) it is evident that shock velocity is given by: ( $u_0 = 0$ )

$$U = \frac{1}{\rho_0} \left( \frac{\sigma}{v_0 - v} \right) \quad (1)$$

Hence, shock velocity is pro-

portional to the square root of the negative slope of the straight line joining the initial and final states. This relation allows the range of stresses for which single shock fronts are unstable to be easily determined. Thus, Point B is the critical stress for which the second front just overtakes the first. For a final state C the shock consists of two fronts, of which the velocity of the first is related to the slope AB, and the velocity of the second to the slope BC.

In the above model, the slope of the elastic forerunner in the Hugoniot plane is constant. It is usually observed however, that the slope of the elastic forerunner in the Hugoniot plane is not constant but that the locus of states has some positive curvature. This is believed to be a result of the large principal stresses and the accompanying deviations from Hooke's law.

The terminology of the various pressure fronts resulting from shock instability is sometimes misleading. The first pressure front is usually called the elastic wave or similar designation. The second pressure front may represent the elastic wave, or a particular phase transition. Because of the uncertainty in separation, phase transitions from yield transitions, the pressure fronts will be designated in the numerical order in which they are recorded, e.g., first wave, second wave.

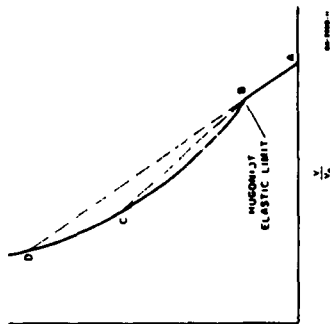


FIG. 1 HUGONIOT EQUATION OF STATE OF A SOLID IN THE VICINITY OF THE YIELD POINT

Determining the most data from observations on a multiple wave system requires that each wave front be observed separately. The following methods were developed during the present project to satisfy this requirement. These methods use inclined mirror and optical lever recording techniques which depend upon changes in reflectivity or turning of a mirror surface.

The arrangements described below are suitable for different purposes, the basic principles and measurements are the same in each application.

The plane-wave pellet arrangement is best used on non-porous materials and is the only one of the methods that can be used on single crystals at the present time. Shock velocities in crystals are more simply expressed along the principal crystallographic directions and in order to profit from this simplicity, the direction of shock propagation and measurement must be along the principal axes. This restriction does not permit wedge methods to be used.

The plane-wave beveled pellet arrangement differs from the plane-wave pellet arrangement in that an additional face is used. This allows a measurement of the shock velocity to be made on the wedge surface, and an impedance-match solution, that does not use the free-surface assumption, can be computed. Measurements and computations made in the plane-wave pellet arrangement are also made on the beveled pellet. The beveled pellet is useful for experiments with porous materials, where the free-surface assumption does not hold, or in instances where it is desired to check the free-surface assumption.

The plane-wave wedge experiments use only the wedge part of the beveled pellet and are useful for measurements in porous rocks for the above reason, and for measurement of shock attenuation.

The two-dimensional wedge experiment is used when feasible because it gives the state of the material at many pressures in one experiment, rather than only one pressure as in the plane-wave experiments.

#### A PELLET METHOD

The pellet method is used for all crystals and nonporous solids. A sample of the material is cemented to a backing plate, and a plane shock wave is driven through the backing plate and into the pellet. The experiment is designed to determine shock wave and particle velocity.

Shock wave velocity is measured by observing the transit time of the shock wave through a known thickness of sample. Particle velocity is determined by measuring the free surface velocity produced upon interaction of the shock wave with a free boundary and converting to particle velocity as discussed above.

An explosive assembly,\* which produces a plane detonation wave, is cemented to one surface of the backing plate; specimen and mirrors are cemented to the other surface (Fig. 2). The backing plate is usually  $\frac{3}{8}$  inch thick and large enough to cover the explosive lens. The materials most commonly used for the backing plates are aluminum, lucite, and laminates of mild steel and lucite. The two surfaces of the plates are cut parallel, lapped, and sometimes polished. The mirrors are made from lucite and aluminized on one side. Dimensions of the specimens are 1 to  $1\frac{1}{2}$  inches square and  $\frac{1}{8}$  to  $\frac{1}{4}$  inch thick.

The mirrors are placed so that the aluminized surfaces are against the backing plate and cemented around the edges; precautions are taken so that no cement is between the aluminized surface and the plate. Figure 3 shows the arrangement.

Figure 4 is a simplified diagram of the interaction of the assembly with a plane shock wave. The diagram does not illustrate the interactions of shock waves with edges or the reflected waves after a surface is reached. The shock front,  $S_1$ , in the backing plate, generated by the explosive lens, travels with a velocity  $U_1$ . Mirrors at A, C, G, along with the aluminized lower surface of the specimen (if the specimen is transparent) record the arrival of the shock wave at the upper surface of the backing plate. This is recorded as a change in the intensity of reflected light when the shock wave destroys the aluminized surface of the mirrors. The planarity of the shock wave can be observed in this manner and corrections made in the data if there is a "tilt" to the shock wave. The reflection of the shock wave at the surface of the backing plate results in the surface traveling at a velocity  $u_1$ . The moving surface turns the inclined mirror and the point of collision is recorded by a change in the intensity of reflected light. The edge of Mirror B touching the backing plate also records the arrival of the shock wave at the surface. The mirror angle is adjusted so that the apparent velocity of the point of collision is supersonic. This

\* Manufactured by Mason and Weager, Inc., Austin, Texas.

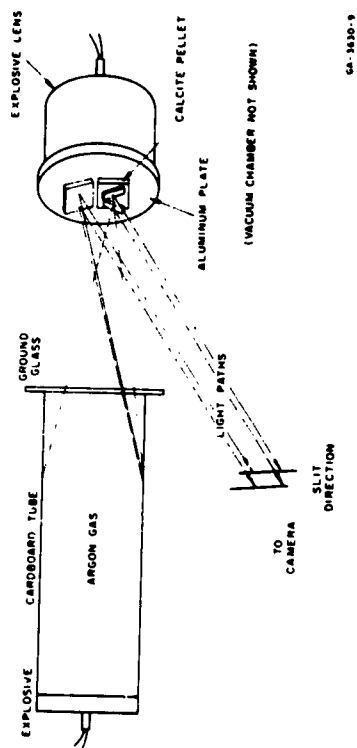


FIG. 2 DIAGRAM OF EXPERIMENTAL SETUP

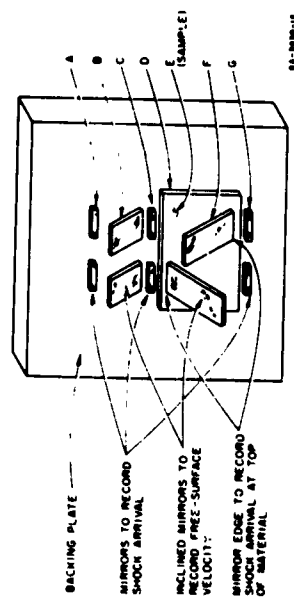


FIG. 3 DIAGRAM OF EXPERIMENTAL ASSEMBLY

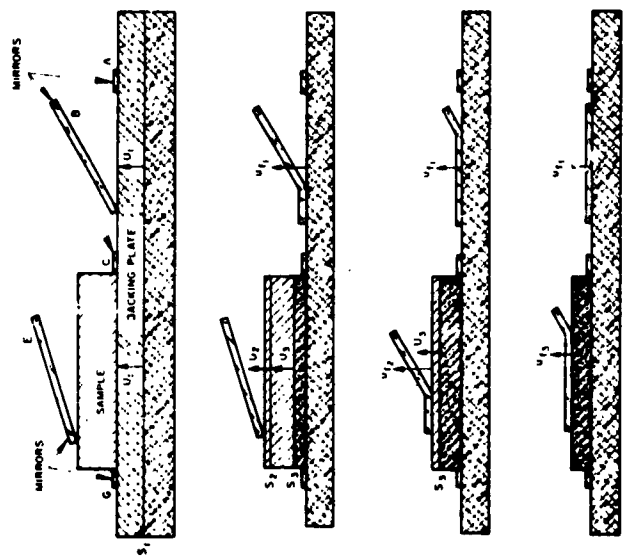


FIG. 4 SIMPLIFIED DIAGRAM OF THE ASSEMBLY UNDERGOING SHOCK LOADING

insures that no signal due to the collision can influence either the specimen or the mirror ahead of the point of collision.

The shock wave traveling in the backing plate reaches the boundary between the plate and specimen and interacts to transmit a shock wave of different pressure into the specimen. The shock wave in the specimen may be unstable and form a double shock,  $S_2$  and  $S_3$ , indicating a phase change or failure at the elastic limit. The two shock waves  $S_2$  and  $S_3$  in the sample travel with velocities  $U_2$  and  $U_3$ . The reflection of the shock wave with velocity  $U_2$  at the surface of the sample accelerates the surface to velocity  $u_{f2}$ , which is much slower than the shock wave velocity, then the shock wave,  $S_3$  with velocity  $U_3$ , overtakes the free surface and further accelerates it to velocity  $u_{f3}$ .

Initially, the inclined mirror on the sample is turned by the surface traveling with velocity  $u_{f2}$ , and if the angle between mirror and pellet surface is  $\alpha$ , the point of intersection of mirror and pellet surface travels along the mirror with apparent velocity  $U_{a1} = u_{f2} \sin \alpha$ . When the second shock accelerates the free surface to velocity  $u_{f3}$ , the apparent velocity,  $U_{a2}$ , is increased to  $u_{f3} \sin \alpha$ . These apparent velocities are recorded with a streak camera as described below. The edge of the inclined mirror that touches the sample also records the arrival of the shock wave at the upper surface of the specimen.

When possible, two separate systems of mirrors are used. This permits two independent measurements to be made, providing a check on the results. Further, the mirrors on the upper surface are inclined at different angles to provide optimum resolution for different parts of the free surface motion.

An argon explosive light source is used to illuminate the mirrors during the experiment. Argon gas, which becomes strongly luminescent when shock loaded, is contained in a cardboard or wooden box with an explosive pad at one end and a glass cover at the other. The glass cover may be etched to diffuse the light or it may contain grid lines and various filters. The argon is allowed to flow through the box to minimize dilution by air; the duration of light is about 50 microseconds.

Figure 2 illustrates the basic experimental setup. The light source is properly timed to illuminate the specimen and mirrors during the interval of the experiment. The mirrors are oriented so as to direct light from the edges of the light source toward the camera, and they

are turned into the light source by the arrival of the shock wave. This results in a change in the intensity of the light reflected by the mirrors.

Changes in light intensity are recorded by a streak camera which uses an air turbine to rotate, at 2000 rps, a mirror past a strip of 35-mm film arranged circumferentially in the camera. A 0.1-mm slit of light from the shot assembly is swept along the film to produce a one-dimensional time plot of the light and dark events contained in the field of view of the slit. The writing speed of the rotating mirror is 3.8 mm/ $\mu$ sec and time resolutions of 0.01  $\mu$ sec are possible.

When two sets of mirrors are used on the specimen, a slit across each set sweeps along the film to give a double exposure of the events. It is still possible to separate the events from each mirror provided proper exposure is made.

Figure 5 is a streak camera photograph from a Z-cut calcite experiment. Differences in light intensity demarcate the records from the two slits.



FIG. 5 STREAK CAMERA PHOTOGRAPH FOR A Z-CUT CALCITE CRYSTAL

The photograph has been retouched at I, to D to H to show slight changes in intensity more clearly.

At each slit differences in light intensity record the arrival of the shock wave. Figure 6 is a diagram of the information contained on the photograph. At slit 1, the arrival of the shock wave at the surface of the driver plate is recorded by A, B, C, D, E. The slope of the trace at B records the free-surface velocity of the driver plate. The distance between D and E (time interval  $t_0$  to  $t_1$ ) records the transit time of the shock wave in the caliche. E records the arrival of the shock wave at the upper surface of the caliche. The slope from E to  $E_1$  records the free-surface velocity of the first wave in caliche; the slope from  $E_1$  to  $E_2$  provides a measure of the free-surface velocity of the second wave. Similar points are indicated for the other slit.

The data, which is obtained from the interpretation of the film, are angles of the inclined mirror traces and indications of the successive shock arrival at the interfaces. These data will be used in computing the necessary parameters of Eqs. 1. The computation described below is taken from a report by Fowles.<sup>3</sup>

The free-surface velocities,  $u_f$ , were computed by means of the relation:

$$u_f = \frac{\tan \alpha}{MF \tan \gamma} \quad (4)$$

where  $\alpha$  is the angle of the inclined mirror with respect to the quartz free surface,  $\gamma$  is (approximately) the angle of the trace on the film with respect to the space axis,  $M$  is the magnification or ratio of distance on the film to the corresponding distance on the shot, and  $F$  is the writing speed of the camera. This relation can be verified by reference to Fig. 7 which shows the correspondence of distances on the film to times and distances at the shot.

The velocities deduced from this relation require small corrections because of tilt in the incident shock, designated by  $\theta$  in Fig. 7, and because of small errors in alignment within the camera. The alignment error results from lack of precise orthogonality between the slit direction and sweep direction. The departure from orthogonality is designated by  $\delta$ .

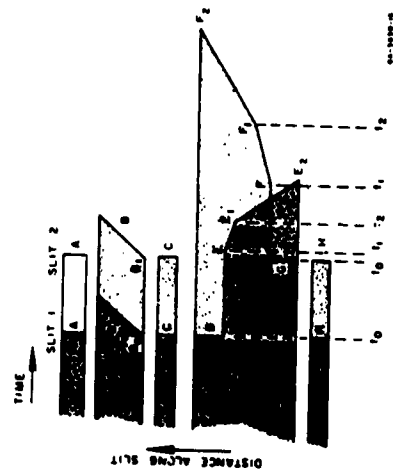


FIG. 6 DIAGRAM OF THE STREAK CAMERA PHOTOGRAPH

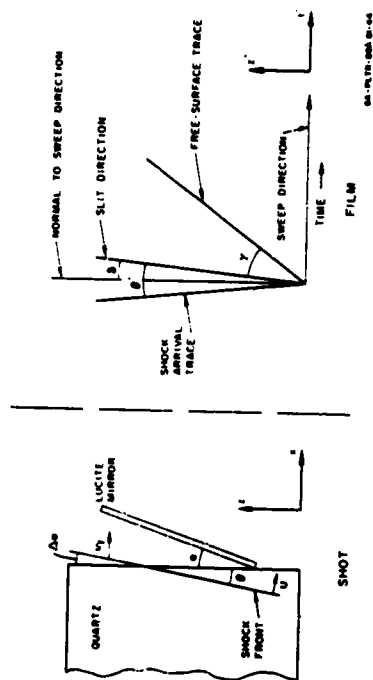


FIG. 7 CORRESPONDENCE OF TIMES AND DISTANCE AT SHOT TO DISTANCES ON STREAK RECORD

The correction to  $\alpha$  due to shock tilt is given by:

$$\Delta\alpha \approx \frac{\tan \alpha}{\tan \gamma} b' \quad (5)$$

where  $b'$  is the angle of shock tilt as measured on the film, and  $\alpha$  is the mirror angle.

The correction to  $\gamma$  due to a nonzero value of  $b$  is:

$$\tan \gamma' = \tan \gamma' \sec b(1 - \tan \gamma' b) \quad (6)$$

where  $\gamma'$  is the angle of trace with respect to the slit direction.

The procedure was, therefore, to determine  $\gamma$  from measured values of  $\gamma'$  and  $b$  by Eq. (6), to compute  $\Delta\alpha$  by Eq. (5), and finally, to compute  $u_f$  by Eq. (4) with  $\alpha = \alpha_0 + \Delta\alpha$ , where  $\alpha_0$  is the original mirror angle. In practice, the corrections to Eq. (4) resulting from replacement of  $\alpha_0$  by  $\alpha$ , and  $\gamma'$  by  $\gamma$  were quite small.

The velocity of the first shock is computed immediately from the observed travel time,  $(t_1 - t_0)$ , and the known pellet thickness. An "average" velocity for the second shock is computed from the observed travel time,  $(t_2 - t_0)$ , and the effective pellet thickness, adjusted for the displacement of the specimen free surface prior to arrival of the second shock. Thus, to a first approximation the second shock velocity,  $u_2$ , is given by:

$$u_2 = \frac{d + u_{f1}(t_2 - t_1)}{t_2 - t_0} \quad (7)$$

where  $d$  is pellet thickness,  $u_{f1}$  is the free-surface velocity due to the first shock, and  $t = (\text{distance on film})/(\text{writing speed})$ .

The experimental precision, based on assembly tolerances, camera resolution, and film reading errors is estimated to be  $\pm 1\%$  in shock velocity and  $\pm 5\%$  in free-surface velocity. Most of the error in free-surface velocity is due to uncertainty in the reading on the film of angle  $\gamma$ . This error is estimated to be less than  $1^\circ$ .

An impedance match solution may be used to check the results. This solution is described in the following section.

## B. BEVELED PELLET METHOD

The Beveled Pellet Method differs from the method above by using an inclined surface as well as the surface that is horizontal to the backing plate. From the inclined surface, additional values of shock velocity are measured and used in an impedance match solution to provide check on the previous results. This type of experiment is suitable for porous or other materials in which the validity of using the free-surface approximation is questioned.

A schematic diagram of the experimental arrangement is given in Fig. 8. The explosively driven plane wave moves through the backing plate and into the beveled rock pellet. The mirrors and the polished backing plate are illuminated by the light from an argon light source similar to that described above. The only difference is that a grid of clear lines spaced 2 mm apart in a background of 0.6 photographic density is placed on the face of the argon tube. The shot is viewed through the slit of a streak camera so that the grid image appears as a series of light and dark spots. The image is swept along the film, producing parallel lines such as those at the left of Fig. 9. If a reflecting surface changes to a diffuse reflector, the images disappear. The wave arrival at the backing plate, visible in the regions A, and the arrival of the free surface of the backing plate at the tilted mirrors at B are visible in Fig. 9 for this reason. If reflectivity changes, light intensity changes. The mirror along the beveled pellet edge at C and the tilted mirror on the pellet at D both drop sharply in reflectivity to signal respectively the wave arrival and the arrival of the moving free surface of the pellet. A third effect by which arrivals could be noted is the displacement of images produced by any rotation of a reflecting surface.

Camera writing speed and image magnification are measured so that Fig. 9 may be used as a time-distance plot. Apparent velocities are obtained from the slopes of the streak camera traces. The average shock velocity,  $U$ , is obtained by dividing the pellet thickness by the transit time, indicated by the arrival at the backing plate and the point at which the smear from the large tilted mirror at D begins to cut off. Another value of  $U$  is obtained from the apparent wave velocity  $U_{app}$  along the mirror on the beveled part of the pellet at C in Fig. 9.

$$U = U_{app} \tan \theta \quad (8)$$

where  $\theta$  is the measured angle of pellet level. These two velocity determinations differed by 0.2 percent on the shot of Fig. 9. The free-surface velocities of the aluminum backing plate and of the pellet were determined from the apparent velocities of the appropriate traces and from the measured angles  $\alpha$  of the tilted mirrors by means of the formula,  $U_p = U_{app} \tan \alpha$ . This is the same as in the Pellet Method.

The impedance-match solution for the stress-particle velocity state in the specimen is obtained by the method shown in Fig. 10. The curve OA is the previously determined locus of points which can be attained by passing a shock through the backing plate of 2024 aluminum. The point A represents the state behind the shock which is incident on the aluminum free surface and on the pellet.

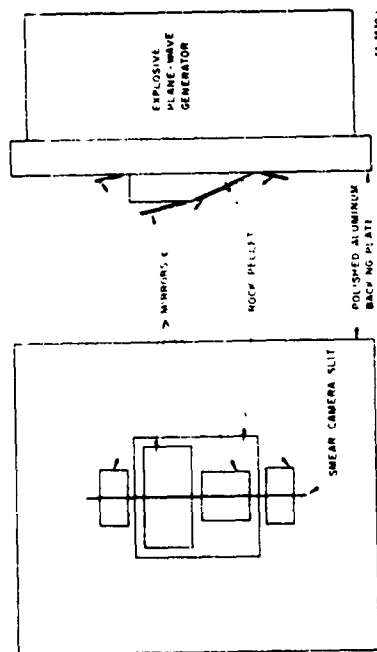


FIG. 8 SCHEMATIC OF BEVELED PELLET EXPERIMENT

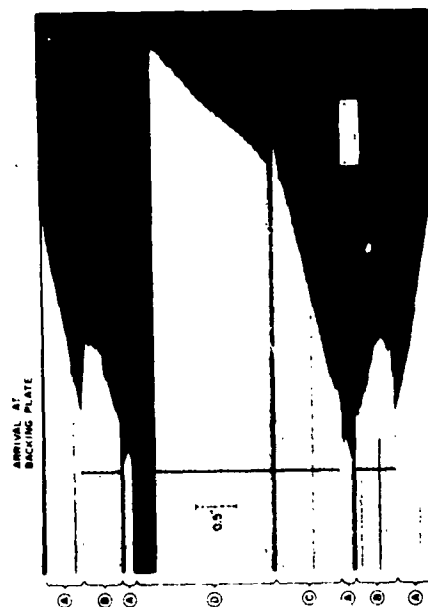


FIG. 9 REVELED PELLET RECORD - SANDSTONE (Shot No. 78s1)

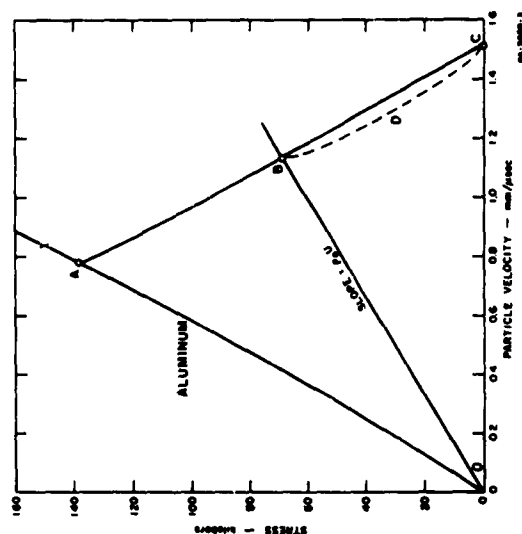


FIG. 10 GRAPHICAL INTERPRETATION OF BEVELED PELLET RECORD (Shot No. 78s1)



The particle velocity,  $u$ , is obtained from the measured free-surface velocity,  $u_f$ , of the aluminum plate by using the relation  $u = (1/2)u_f$ . A reflected wave is generated when the shock reaches the interface between the aluminum backing plate and the pellet. The states which can be attained by the reflected wave can be calculated from the known properties of aluminum; they are very close to AB, a mirror image of the curve OA. Since normal stress and particle velocity must be continuous across the interface, the state in the sample must lie on AB. From the equation for conservation of momentum,  $\sigma = \rho_0 U u$ , the state in the specimen must also be on a straight line with a slope  $(\sigma/u) = \rho_0 U$ . The intersection of this line with AB determines H, the state in the pellet. The associated compression and specific energy may be calculated from the equations for conservation of mass and energy across the shock front.

The free-surface velocity of the pellet in the example of Fig. 10 was 1.51 mm/ $\mu$ sec. This value gives a point at C on the locus of states attainable by a reflected rarefaction wave in the rock. Because of the porosity, the free-surface approximation was very poor for this sandstone; free-surface velocity was only 1.34 times particle velocity. If the rarefaction wave reflected from the free surface of the rock pellet is regarded as a sharp-fronted wave with velocity,  $-U_r$ , it adds a particle velocity,  $u_r = u_f/2 = u$ . The stress drop across the wave front is

$$\sigma_r = \rho(U_r + u)u, \quad (9)$$

The free-surface boundary condition of zero stress forces the stress drop across the reflected wave to be equal in magnitude to the stress rise,  $\sigma$ , across the incident wave, and opposite in sign; therefore  $\rho(U_r + u)u = -\sigma$ . The velocity of the reflected wave relative to the particles it is moving into is then,

$$(U_r + u) = -\frac{\sigma}{\rho u}, \quad (10)$$

This quantity is just  $1/\rho$  times the negative slope of the chord BC in Fig. 10. It equals 5.81 mm/ $\mu$ sec, almost twice the 3.06 mm/ $\mu$ sec velocity of the incident wave. The velocity of 5.81 mm/ $\mu$ sec is close to the velocity in crystal quartz so that it appears that the original porosity has negligible effect on the velocity of the reflected wave.

### C. PLANE-WAVE WEDGE METHOD

A wedge of the sample is placed on the backing plate instead of the leveled pellet and the experiment is assembled in a similar manner. The only solution is obtained by the impedance-match method. Two different metals were used as mirrors on each shot so that a check could be obtained by having two different impedance-match solutions.

A schematic diagram of the plane-wave wedge arrangement is shown in Fig. 11. The explosively driven plane wave waves from the backing plate into the small wedges of rock and aluminum. The shot is illuminated by an argon light source, on the face of which a grid of clear lines spaced  $1/8$  inch apart on an opaque background is placed. The shot is viewed through two slits by the streak camera. The sets of grid lines for the two slits are offset from one another by  $1/8$  inch so that the trace from one slit do not overlap the traces from the other slit. In addition, the shot is photographed in color with a colored filter over one slit so that traces on the resulting smear record can be followed even should they cross.

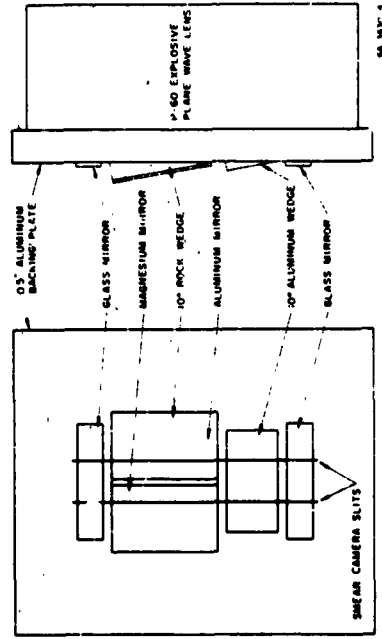


FIG. 11 SCHEMATIC OF PLANE-WAVE WEDGE EXPERIMENT

with the previously determined  $v-u$  curve of aluminum provides a check on the calculations and measurements.

The wave arrivals at the mirrors on the rock show a two wave system in the rock pellet with the first wave indicated by the dashed lines at E and F in Fig. 12. The  $v-u$  state of the first wave cannot be determined by the usual impedance-match solution of Fig. 10. From the apparent velocities of arrivals, velocities of the first and second waves were calculated as  $c_1 = 5.58$  and  $c_2 = 4.96$  km/sec. The free-surface approximation is used to obtain particle velocities in the aluminum and magnesium mirrors on the rock pellet, giving points A and B on the known  $v-u$  locus of these metals shown in Fig. 13. A line on the locus of states attainable

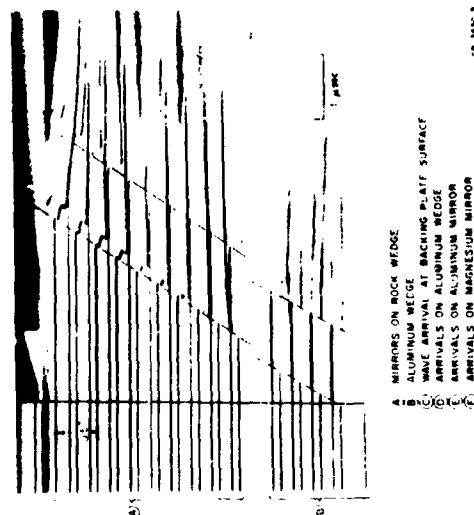


FIG 12 PLANE-WAVE WEDGE RECORD OF SIOUX QUARTZITE

The reflecting surfaces of the aluminum wedge and of the two mirrors on the rock pellet turn upon arrival of the wave. Images of the light source grid are displaced as shown in the record of Fig. 12.

The wave velocities in the aluminum wedge and rock are calculated as in the beveled pellet method. The normal component of free-surface velocity,  $u_n$ , is obtained from the magnitude,  $a$ , of the displacements of the images of the light source grid,  $u_n = (a/2d)/U_{app}$ , where  $d$  is the normal distance of the grid from the shot and  $U_{app}$  is the apparent velocity determined as before by the slope of the trace. Details of this optical lever technique are given by Fowles.<sup>6</sup>

The wave arrivals and displacements on the aluminum wedge at D give wave velocity and free-surface velocity in the backing plate. Use of the free-surface approximation gives the stress-particle velocity point at D in the graphical solution of Fig. 13. The fact that this point agrees

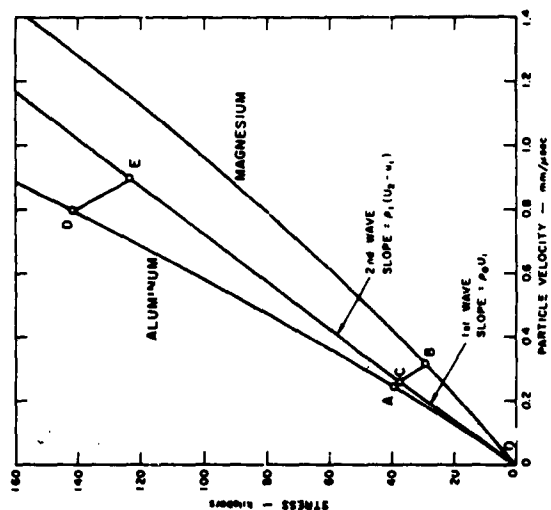


FIG 13 GRAPHICAL INTERPRETATION OF PLANE-WAVE WEDGE EXPERIMENT

by reflected shocks in the rock and B lies on the locus of reflected refractions. Since A and B are close to one another, the straight line AB is a good approximation to the curve of reflected wave states of the rock Hugoniot. The intersection at C of AB with the line from the origin of slope  $\rho_0 c_0$  determines the state behind the first wave in the quartzite pellet of Figs. 10 and 11.

The state behind the second wave on the other hand, can be determined from an ordinary impedance-match solution. Thus, state E is determined by the intersection of the locus of reflected rarefactions from the state D of the aluminum backing plate with the line of slope  $\rho_1(u_2 - u_1)$  passing through the state C of the first wave. This solution for the second wave at E should also be obtained in the same manner as for the first wave, the intersection of the line connecting the states behind the second wave in the aluminum and magnesium mirrors with the line of slope  $\rho_1(u_2 - u_1)$ . The agreement between the two solutions provides a check on the results.

The slope of the line connecting the states on the aluminum and magnesium mirrors leads to an approximate value for sound speed behind the shock front for reasons given in the discussion of the beveled pellet method.

## D TWO-DIMENSIONAL WEDGE EXPERIMENT

The two-dimensional wedge geometry of Fig. 14 has two advantages over the plane-wave arrangements described above. Each shot yields data for a range of stress instead of just one point, and low stressers can be more easily reached in the wedge than in the plane-wave experiments. The wedge geometry was first used by Katz, *et al.*<sup>3</sup>

As shown in Fig. 10, a detonation front progresses in an explosive slab with constant velocity,  $U_0$ , inducing a shock wave in the specimen. The shock decays as it progresses into the wedge so that a range of stresses will be observed at the wedge face. When the detonation wave has traveled far enough, the shock wave will be steady in time, i.e., the point of intersection of the shock with any horizontal plane will travel with an apparent velocity equal to detonation velocity. Under these conditions it is apparent from the figure that shock velocity,  $U_s$ , at any point, is given by:

$$U_i = U_0 \sin \alpha - U_{\infty} \sin \gamma \quad (11)$$

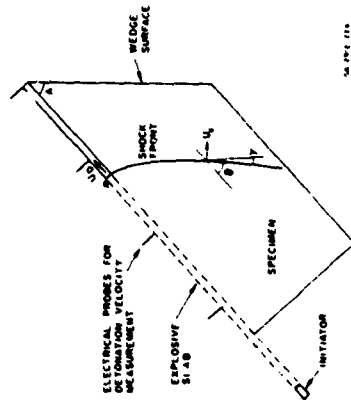


**FIG. 14 SIDE VIEW OF TWO DIMENSIONAL WEDGE EXPERIMENT**

where  $C_D$  is detonation velocity and  $C_{app}$  is the apparent velocity with which the shock intersects a plane parallel to the wedge face.

Moreover, since

(12)

$$\sin \psi = \frac{c_{app}}{v_B} \sin (\theta - \psi) \quad (13)$$

from which

$$\cot t = \cot A + \frac{u_D}{u_{\text{app}} \sin A} \quad (14)$$

thus, when  $U_{\text{app}}$ ,  $U_D$ , and  $A$  are measured,  $U_n$  can be calculated at any point on the wedge surface.  $U_{\text{app}}$  is obtained from the streak camera record of the arrival of the wave at the wedge surface. At the same time, the component of free-surface velocity normal to the wedge face is measured by the method described below.

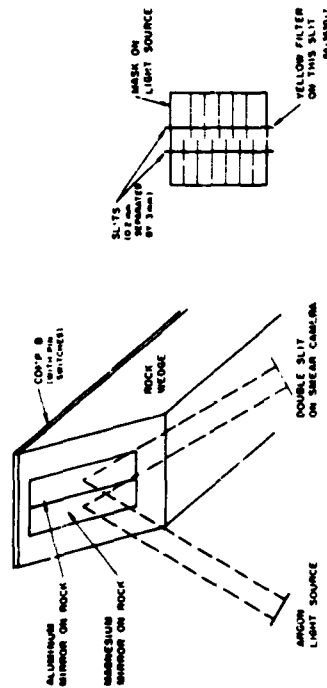


FIG. 13 SCHEMATIC OF TWO MIRROR WEDGE EXPERIMENT

Two mirrors are placed on the wedge face as shown in Fig. 13. The normal component of free-surface velocity at each point covered by a grid line is obtained by the optical lever arm technique described in the preceding section. The free-surface velocity approximation is then used to obtain particle velocity for each mirror as a function of depth in the wedge. At any depth, particle velocity is read from plots of the mirror data. The particle velocity in the rock at that depth is graphically obtained in the same way as point C in Fig. 13. The process can be repeated for multiple wave systems by applying the jump conditions across each wave front in turn.

The two-dimensional method was used to generate most of the data on the polycrystalline rocks. The two plane-wave arrangements are easier to interpret and are used to spot-check the results of the two-dimensional method. Appendix C contains further details about the reduction of data from the two-dimensional wedge experiments.

### III RESULTS

Values of shock parameters obtained from shock wave experiments on quartz, calcite, and the related rocks are listed in Tables III, IV, V, VI. Table I lists the experiments on each rock and Table II lists pertinent information on each rock. Diagrams of the states of stress-particle velocity and stress-volume for the various materials are shown in Figs. 16-19, 21-25.

#### A. QUARTZ

Table III records all of the data on quartz measured at NII. The measurements on quartz were made by Fowler,<sup>6</sup> with the exception of Shot 8504.

Figure 16 displays all the known shock wave data on quartz. Agreement between Fowler's<sup>6</sup> and Wackerle's<sup>3</sup> measurements is generally good. The scale in Fig. 16 is expanded in Fig. 17 and displays the shock wave data on quartz up to 250 kilobars. Agreement between Fowler's<sup>6</sup> and Wackerle's<sup>3</sup> measurements is more apparent. The only disagreement in data is for the second wave in Z-cut quartz. Data by Fowler lie about 25 kilobars above data by Wackerle. Shot 8504 was designed on this project to specifically measure the shock parameters of the second wave in Z-cut quartz. The result agrees with data by Fowler.

#### B. QUARTZ ROCKS

Table IV and part of Table V list the values obtained from shock wave experiments; significant data on stress-particle velocity and stress-volume relations are displayed graphically in Figs. 18 and 19 respectively.

Comparisons are made of the data from rocks that differ in only a few of the initial state parameters so that any differences in shock wave data can then be attributed to variations in these initial parameters. The reader is referred to Table II or Appendix A and B for information on the differences and similarities of each rock, and the parameters that affect porosity.

Table I  
SUMMARY OF EXPERIMENTS

MATERIAL	SERIAL NO.	GEOMETRY	POSSIBLE NAME (kilobars)	EXPERIMENTAL (kilobars)	NOTES
Quartz	8244	Plane-wave pellet	230 to 230	170	2-ent pellet
Archeanite	8238	Plane-wave beveled-pellet	82 to 82	82	
	8278	Plane-wave beveled-pellet	97 to 125	97	
	8272	Plane-wave beveled-pellet	21 to 41		
	8275	Two-dimensional wedge	28 to 41		
	8289	Two-dimensional wedge	28 to 41		
Siene Quartzite	7995	Plane-wave wedge	231		
	7996	Two-dimensional wedge	18 to 182		
Berkshire Quartzite	7999	Two-dimensional wedge	65 to 68	36	
Coconino Sandstone	7715	Plane-wave pellet	133		Perpendicular to bedding
	7716	Plane-wave pellet	146		
	7869	Plane-wave wedge	69 to 67		
	7861	Plane-wave beveled-pellet	121		
	8162	Plane-wave wedge	121		
	8164	Plane-wave beveled-pellet	121		
	8169	Plane-wave wedge	7 to 91		
	8163	Two-dimensional wedge	48 to 56		
	8170	Two-dimensional wedge	44 to 49		
	8172	Two-dimensional X-ray	2 to 49		
Calcite	8449	Plane-wave pellet	29 to 92	29	Clearance-cut Calcite
	8451	Plane-wave pellet	22 to 84	22	Clearance-cut Calcite
	8454	Plane-wave pellet	135		2-ent Calcite (results are)
Yule Marble	7795	Plane-wave wedge	176		Poor results
	7796	Plane-wave beveled-pellet	121	12	
	8281	Plane-wave beveled-pellet	121		
	8217	Plane-wave wedge	253		
	7977	Two-dimensional wedge	28 to 129	12, 16, 24	Uncertained
	8218	Two-dimensional wedge	18 to 132	4, 9, 15	
Spargen Limestone	8679	Plane-wave beveled-pellet	90		
	8680	Plane-wave beveled-pellet	261		
	8136	Plane-wave wedge	41	2	
	8145	Plane-wave beveled-pellet	271		
	8271	Plane-wave beveled-pellet	44		
	8148	Two-dimensional wedge	29 to 39	17	
	8149	Two-dimensional wedge	5 to 72	2	
	8252	Two-dimensional wedge	61 to 135	3	
	8268	Two-dimensional wedge	61 to 135		Pressure not readable at magnification

Table II  
SUMMARY OF ROCK INFORMATION

NAME	GRAIN SIZE (mm)	COMMENT	PERCENTAGE (%)	DENSITY (g/cc)	COMMENTS
QUARTZ ROCKS					
Arkansas Microsilite	0.01	Mass observed (if no $\text{H}_2\text{O}$ )	~0.2	2.649	Pure silica, and no reaction observed. Some banding.
Barro Quartzite	0.1-0.2	Mass observed	<1	2.58	98% qtz.; relic banding but diffuse and slight.
Sierra Quartzite	0.6	Qz. overgrowth	<1	2.636	97% qtz.; hematite dust between grains and irregularly oriented (no orientation study made.)
Cornwall Sandstone	0.117	High to moderate siliceous overgrowth (20%)	15-25	2.26	97% qtz.; laminated to bedding and "diffuse"
CALCAREOUS ROCKS					
Yule Marble	0.2-0.4	Mass	<1	2.69	Increase in size of grains; increased orientation of grains.
Spargen Limestone	0.3-0.4	0.2-0.3	15.1	2.30	Not oriented fossiliferous

Table III  
SUMMARY OF EXPERIMENTAL DATA FOR QUARTZ<sup>4</sup> AND CALCITE

SHOT NO.	EXPLOSIVE	ORIENTATION	PELLET THICKNESS (cm)	ARRIVAL TIMES		PRE-SURFACE VELOCITIES		FIRST SHOCK				SECOND SHOCK			
				$t_1 - t_0$ ( $\mu$ sec)	$t_2 - t_0$ ( $\mu$ sec)	$U_1$ (cm/sec)	$U_2$ (cm/sec)	Shock Velocity (cm/sec)	Particle Velocity (cm/sec)	$V_s/V_p$ ( $\mu$ sec)	$V_s/V_p$	Shock Velocity (cm/sec)	Particle Velocity (cm/sec)	Screen $U_2$ ( $\mu$ sec)	$V_s/V_p$
QUARTZ															
5648	P-40 lens	X(- to +)	6.378	1.051	1.296	0.492	1.62	6.03	0.346	55.5	0.9426	5.05	0.810	117.0	0.8495
5907	P-40 lens	X(- to -)	6.388	1.075	1.308	0.497	1.62	5.94	0.402	62.7	0.9320	5.03	0.810	117.4	0.8500
5806	P-40 lens	X(+ to -)	6.393	1.078	1.322	0.754	1.66	5.91	0.377	59.4	0.9364	4.99	0.758	110.1	0.8403
5921	P-40 lens	X(+ to -)	6.380	1.079	1.146	(0.704)	2.630	5.91	0.393	(61.8)	(0.9335)	4.97	(0.828)	118.1	0.8444
5921	P-40 lens	X(- to +)	6.371	1.040	1.144	0.497	2.63	5.94	0.347	(62.4)	(0.9421)	5.46	1.315	158.8	0.7486
5920	P-40 lens	Z(- to +)	6.380	0.876	1.137	1.40	2.63	7.28	0.698	135.1	0.9041	5.65	1.313	199.9	0.7702
6009	P-40 lens	Z	6.358	1.058	1.363	0.819	1.43	6.01	0.410	65.3	0.9320	4.85	0.713	103.7	0.8684
5997	P-40 lens	Z	6.380	0.893	1.190	1.12	3.00	7.15	0.548	106.6	0.9275	5.42	not observed	not observed	0.7411
7163	P-40 lens	Z	6.380	0.914	1.284	1.40	(2.63)	7.33	0.700	136.1	0.9046	5.72	(1.32)	127.2	(0.7934)
7394	P-40 lens	Z	6.396	0.914	1.024	1.09	1.58	7.22	0.520	99.8	0.9240	4.14	0.79	127.4	0.8598
7394	P-40 lens	Z	6.407	0.899	1.330	1.27	2.72	7.35	0.625	123.6	0.9139	5.26	1.16	195.8	0.8124
7395	P-40 lens	Z	6.411	0.882	1.330	1.40	1.60	6.07	0.418	67.7	0.9308	4.77	0.800	114.9	0.8495
8504	P-40 lens	Z	6.401	0.913	1.252	1.38	2.68	7.22	0.609	132.4	0.9068	5.64	1.34	227.5	0.7857
CALCITE															
8448	P-40 lens	Cleavage	9.190	1.321	1.889	0.302	1.272	6.955	0.151	28.5	0.9783	4.96	0.636	91.7	0.8796
8461	P-40 lens	Cleavage	9.246	1.297	2.043	0.227	1.233	7.126	0.114	22.0	0.9841	4.61	0.616	84.2	0.8739
8504	P-40 lens	Z	10.900	2.372	2.388		1.383		not observed	not observed		4.85	0.651	85.7	0.8659
	AI driver		10.900	2.388			2.032		not observed	not observed		4.82	1.016	132.7	0.7890

<sup>a</sup> Data except Shot 8504 from Reference 6.  
( ) points in parentheses are less reliable.

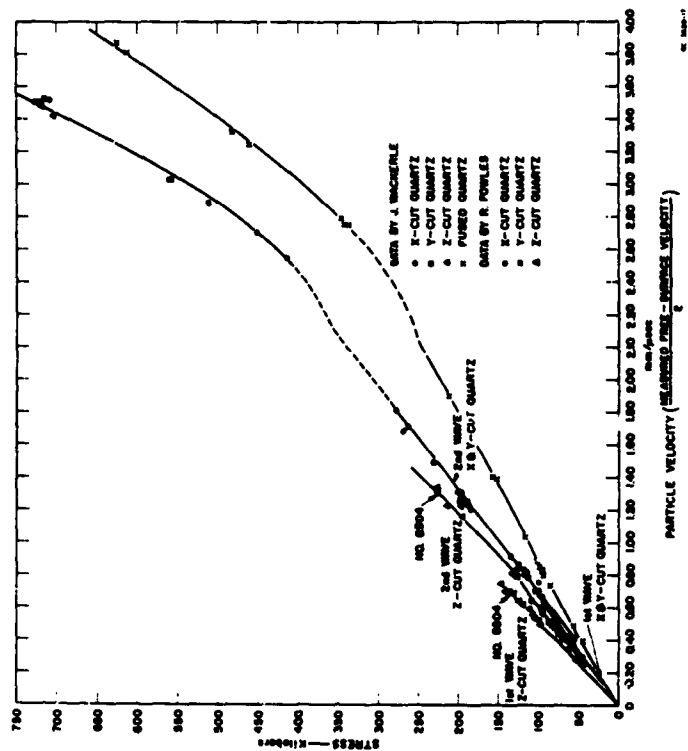


FIG. 16 STRESS vs. PARTICLE VELOCITY FOR QUARTZ



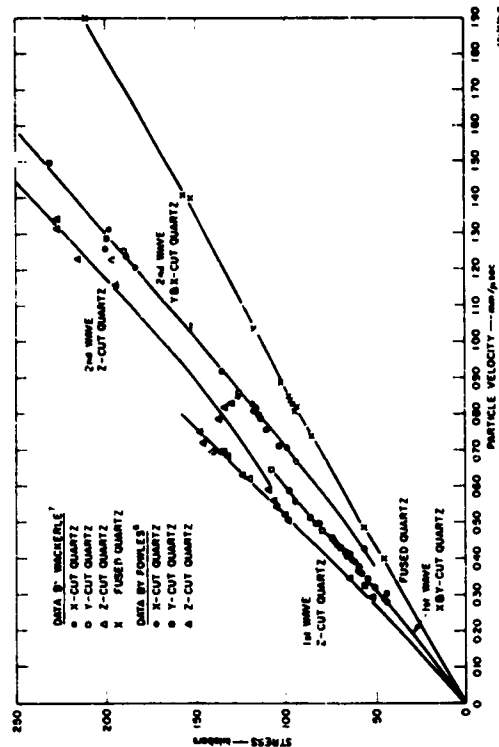


FIG. 17 STRESS vs. PARTICLE VELOCITY FOR QUARTZ

Table IV  
SUMMARY OF DATA FOR QUARTZ ROCKS, TWO-DIMENSIONAL WEDGE EXPERIMENTS

Rock	Specimen No.	ROCK PARAMETERS			SHOCK PARAMETERS										Wave	Notes
		Specimen Dimensions	Explosive	Thick-ness (in.)	Specimen Density (g/cc)	Depth in Rock (in.)	Wave Velocity (in./ms)	Wave Velocity (in./ms)	Wave Velocity (in./ms)	Wave Velocity (in./ms)	Wave Velocity (in./ms)	Wave Velocity (in./ms)	Wave Velocity (in./ms)	Wave Velocity (in./ms)		
Arkansas Noronolite	8275	A=40.0 B=1.0 C=0.0 D=0.0 E=0.0 F=0.0 G=0.0 H=0.0 I=0.0 J=0.0	Shrapnel (2.500)	0.026	2.649	0.000	7.396	7.396	7.396	7.396	7.396	7.396	7.396	7.396	First wave	none
Arkansas Noronolite	8299	A=40.0 B=1.0 C=0.0 D=0.0 E=0.0 F=0.0 G=0.0 H=0.0 I=0.0 J=0.0	Shrapnel (2.500)	0.100	2.642	0.000	7.375	7.375	7.375	7.375	7.375	7.375	7.375	7.375	First wave	none
Arkansas Noronolite	8300	A=30.7 B=1.0 C=0.0 D=0.0 E=0.0 F=0.0 G=0.0 H=0.0 I=0.0 J=0.0	Comp B (0.25)	0.25	2.642	0.000	7.396	7.396	7.396	7.396	7.396	7.396	7.396	7.396	First wave	none

( ) points in parentheses are less reliable.

Table IV Continued

ROCK PARAMETERS										SOURCE PARAMETERS									
Rock	Shot No.	Specimen Dimensions	Detonation Velocity (m/sec)	Explosive	Specimen Density (g/cc)	Depth in Rock (in.)	Shot Angle (deg)	Shot Velocity (m/sec)	Particle Velocity (m/sec)	Depth $P_0/P$	Stress $\sigma$ (lb)	Volume (cc/g)	Marker	Notes					
															Type	Thick- ness (in.)			
Strom Quartzite	7468	A = 3" Ø B = 2.1" C = 0.5"	7,920	Comp B	2.640	0.238	45.6	2,716	0.264	0.951	29,965	0.361	Al	First wave. ramps 18° stepped  Second wave. ramps 18° stepped  Third wave. ramps 18° stepped					
						0.432	45.7	3,471	0.235	0.956	35,340	0.363	Al						
						0.745	45.7	5,649	0.240	0.962	37,258	0.362	Al						
						1.091	45.5	5,626	0.244	0.962	31,413	0.364	Al						
						1.400	45.0	5,406	0.223	0.963	23,080	0.364	Al						
						1.711	44.8	5,141	0.206	0.962	25,884	0.367	Al						
						2.023	44.3	5,541	0.168	0.962	20,369	0.364	Al						
						2.335	44.1	5,520	0.134	0.975	24,622	0.369	Al						
						2.647	43.7	5,277	0.106	0.980	19,642	0.369	Al						
						2.959	43.7	5,477	0.066	0.987	15,458	0.374	Al						
						3.271	43.6	4,951	0.743	0.856	102,025	0.324	Al						
						3.583	43.6	4,881	0.615	0.880	83,969	0.333	Al						
						3.895	43.5	4,759	0.737	0.852	180,479	0.314	Al						
						4.207	43.4	4,705	0.799	0.837	184,634	0.317	Al						
						4.519	43.4	4,629	0.588	0.897	67,470	0.240	Al						
						4.831	43.0	4,546	0.342	0.931	45,797	0.253	Al						
Furze Quartzite	7469	A = 4.0" Ø B = 2.8" C = 0.5"	7,936	Comp B	2.640	0.238	45.6	3,471	0.253	0.954	37,686	0.361	Al	First wave. ramps 18° stepped Light first peak of second wave record  Third wave. ramps 18° stepped					
						0.432	45.6	5,649	0.219	0.951	47,080	0.352	Al						
						0.745	45.2	5,649	0.209	0.957	33,277	0.362	Al						
						1.091	45.1	5,406	0.227	0.962	28,299	0.367	Al						
						1.400	45.1	5,141	0.174	0.969	28,299	0.367	Al						
						1.711	45.0	5,626	0.144	0.970	24,573	0.367	Al						
						2.023	45.0	5,277	0.104	0.973	19,642	0.369	Al						
						2.335	45.1	5,141	0.075	0.981	14,810	0.364	Al						
						2.647	44.6	5,141	0.055	0.984	48,499	0.358	Al						
						2.959	44.5	5,141	0.038	0.989	24,814	0.364	Al						
						3.271	44.5	5,141	0.028	0.990	24,814	0.364	Al						
						3.583	44.1	4,881	0.022	0.992	22,468	0.365	Al						
						3.895	44.1	4,881	0.017	0.993	22,468	0.365	Al						
						4.207	44.1	4,881	0.013	0.995	22,468	0.365	Al						
						4.519	43.7	4,759	0.010	0.997	22,468	0.365	Al						

( ) Points in parentheses are less reliable.

Table IV Continued

ROCK PARAMETERS										SHOCK PARAMETERS									
Rock	Section Number a = 3.1" b = 4.9" c = 9.9"	Detonation Velocity (in./sec.)	Explosive Type	Thick- ness (in.)	Section Density (g/cc)	Shock Angle (deg.)	Shock Velocity (in./sec.)	Particle Velocity (in./sec.)	Ratio $P_0/P$	Stress (lb.)	Volume (cc/g)	Mass	Notes						
Lucerne Sandstone	B119	7,400	Comp B	0.25	1.992	23.4	3,124	0.428	0.971	4.24	0.43	0.43	First wave. Pressure arrived with small amplitude. Values may be poor.						
						23.4	3,124	0.428	0.971	4.24	0.43	0.43							
						23.4	3,124	0.428	0.971	4.24	0.43	0.43							
						23.4	3,124	0.428	0.971	4.24	0.43	0.43							
						23.4	3,124	0.428	0.971	4.24	0.43	0.43							
						23.4	3,124	0.428	0.971	4.24	0.43	0.43							
						23.4	3,124	0.428	0.971	4.24	0.43	0.43							
						23.4	3,124	0.428	0.971	4.24	0.43	0.43							
						23.4	3,124	0.428	0.971	4.24	0.43	0.43							
						23.4	3,124	0.428	0.971	4.24	0.43	0.43							
						23.4	3,124	0.428	0.971	4.24	0.43	0.43							
						23.4	3,124	0.428	0.971	4.24	0.43	0.43							
						23.4	3,124	0.428	0.971	4.24	0.43	0.43							
						23.4	3,124	0.428	0.971	4.24	0.43	0.43							
						23.4	3,124	0.428	0.971	4.24	0.43	0.43							
Lucerne Sandstone	B143	7,510	Comp B	0.25	2.010	23.4	3,124	0.428	0.995	1.142	0.495	0.495	First wave. Pressure arrived with small amplitude. Values may be poor.						
						23.4	3,124	0.428	0.995	1.142	0.495	0.495							
						23.4	3,124	0.428	0.995	1.142	0.495	0.495							
						23.4	3,124	0.428	0.995	1.142	0.495	0.495							
						23.4	3,124	0.428	0.995	1.142	0.495	0.495							
						23.4	3,124	0.428	0.995	1.142	0.495	0.495							
						23.4	3,124	0.428	0.995	1.142	0.495	0.495							
						23.4	3,124	0.428	0.995	1.142	0.495	0.495							
						23.4	3,124	0.428	0.995	1.142	0.495	0.495							
						23.4	3,124	0.428	0.995	1.142	0.495	0.495							
						23.4	3,124	0.428	0.995	1.142	0.495	0.495							
						23.4	3,124	0.428	0.995	1.142	0.495	0.495							
						23.4	3,124	0.428	0.995	1.142	0.495	0.495							
						23.4	3,124	0.428	0.995	1.142	0.495	0.495							
						23.4	3,124	0.428	0.995	1.142	0.495	0.495							
Lucerne Sandstone	B143	7,510	Comp B	0.25	2.010	23.4	3,124	0.428	0.995	1.142	0.495	0.495	Second wave. Pressure arrived with small amplitude. Values may be poor.						
						23.4	3,124	0.428	0.995	1.142	0.495	0.495							
						23.4	3,124	0.428	0.995	1.142	0.495	0.495							
						23.4	3,124	0.428	0.995	1.142	0.495	0.495							
						23.4	3,124	0.428	0.995	1.142	0.495	0.495							
						23.4	3,124	0.428	0.995	1.142	0.495	0.495							
						23.4	3,124	0.428	0.995	1.142	0.495	0.495							
						23.4	3,124	0.428	0.995	1.142	0.495	0.495							
						23.4	3,124	0.428	0.995	1.142	0.495	0.495							
						23.4	3,124	0.428	0.995	1.142	0.495	0.495							
						23.4	3,124	0.428	0.995	1.142	0.495	0.495							
						23.4	3,124	0.428	0.995	1.142	0.495	0.495							
						23.4	3,124	0.428	0.995	1.142	0.495	0.495							
						23.4	3,124	0.428	0.995	1.142	0.495	0.495							
						23.4	3,124	0.428	0.995	1.142	0.495	0.495							

( ) points in parentheses are less reliable

Table IV Continued

BICE PARAMETERS														SDCS PARAMETERS													
Buck	Shot No.	Specimen Dimensions	Discharge Velocity (m/sec)	Explosive	Thrust Area (in.)	Specimen Density (g/cc)	Depth in Shot (in.)	Shot Velocity (ft/sec)	Shot Angle (deg)	Particle Velocity (ft/sec)	Mass P <sub>0</sub> /P	Stroke (in.)	Volume (cc/g)	Miner	Notes												
Concussion Sandstone	8163 (cont)	A=20.0" B=5.0" C=11.5"	7.910	Camp B	0.25	2.010	0.545	793	16.0	0.803	0.650	17.198	0.323	Al	Second wave												
							0.415	189	16.0	0.406	0.406	0.415	0.406	Al													
							0.452	105	15.4	0.508	0.758	21.528	0.377	Al													
							0.706	133	13.9	0.887	0.745	22.338	0.371	Al													
							0.723	128	12.8	0.913	0.527	30.745	0.354	Al													
							0.723	128	12.8	0.913	0.527	30.745	0.354	Al													
							0.875	133	13.9	1.007	0.764	(14.292)	0.403	Al													
							0.875	133	13.9	1.007	0.764	(14.292)	0.403	Al													
							1.091	125	12.5	1.250	0.557	23.425	0.358	Al													
							1.232	117	11.7	1.411	0.470	(26.717)	0.433	Al													
Concussion Sandstone	8209	A=20.0" B=5.0" C=11.5"	7.099	Sheet B15000	0.060	2.021	0.842	330	7.1	0.008	0.997	0.997	0.491	Al	First wave												
							0.676	272	7.3	0.001	0.999	0.107	0.492	Al													
							0.716	253	7.3	0.029	0.999	0.1393	0.489	Al													
							0.811	245	7.3	0.060	0.999	0.161	0.487	Al													
							0.911	246	7.3	0.127	0.991	1.765	0.488	Al													
							0.943	229	7.3	0.093	0.995	0.165	0.479	Al													
							0.958	247	7.3	0.096	0.970	5.340	0.478	Al													
							0.989	249	7.3	0.249	0.968	5.340	0.478	Al													
							0.923	8.6	1.067	0.254	7.60	6.468	0.378	Al													
							0.927	8.7	1.076	0.350	7.716	7.916	0.361	Al													
							0.977	11.8	1.171	0.224	6.437	54.332	0.215	Al													
							0.987	11.8	1.178	0.394	6.296	39.367	0.231	Al													
Concussion Sandstone	8278	A=17.0" B=5.0" C=11.4"	8.072	Camp B	1.00	2.067	0.411	1495	27.2	1.170	0.630	100.371	0.320	Al	Second wave												
							0.315	269	27.2	0.444	(10.788)	(99.345)	0.342	Al													
							0.412	253	27.2	0.446	(10.684)	(99.345)	0.340	Al													
							0.412	253	27.2	0.446	(10.684)	(99.345)	0.340	Al													
							0.412	253	27.2	0.446	(10.684)	(99.345)	0.340	Al													
							0.412	253	27.2	0.446	(10.684)	(99.345)	0.340	Al													
							0.412	253	27.2	0.446	(10.684)	(99.345)	0.340	Al													
							0.412	253	27.2	0.446	(10.684)	(99.345)	0.340	Al													
							0.412	253	27.2	0.446	(10.684)	(99.345)	0.340	Al													
							0.412	253	27.2	0.446	(10.684)	(99.345)	0.340	Al													
							0.412	253	27.2	0.446	(10.684)	(99.345)	0.340	Al													
							0.412	253	27.2	0.446	(10.684)	(99.345)	0.340	Al													
							0.412	253	27.2	0.446	(10.684)	(99.345)	0.340	Al													
							0.412	253	27.2	0.446	(10.684)	(99.345)	0.340	Al													
							0.412	253	27.2	0.446	(10.684)	(99.345)	0.340	Al													
							0.412	253	27.2	0.446	(10.684)	(99.345)	0.340	Al													
							0.412	253	27.2	0.446	(10.684)	(99.345)	0.340	Al													
							0.412	253	27.2	0.446	(10.684)	(99.345)	0.340	Al													
							0.412	253	27.2	0.446	(10.684)	(99.345)	0.340	Al													
							0.412	253	27.2	0.446	(10.684)	(99.345)	0.340	Al													
							0.412	253	27.2	0.446	(10.684)	(99.345)	0.340	Al													
							0.412	253	27.2	0.446	(10.684)	(99.345)	0.340	Al													
							0.412	253	27.2	0.446	(10.684)	(99.345)	0.340	Al													
							0.412	253	27.2	0.446	(10.684)	(99.345)	0.340	Al													
							0.412	253	27.2	0.446	(10.684)	(99.345)	0.340	Al													
							0.412	253	27.2	0.446	(10.684)	(99.345)	0.340	Al													
							0.412	253	27.2	0.446	(10.684)	(99.345)	0.340	Al													
							0.412	253	27.2	0.446	(10.684)	(99.345)	0.340	Al													
							0.412	253	27.2	0.446	(10.684)	(99.345)	0.340	Al													
							0.412	253	27.2	0.446	(10.684)	(99.345)	0.340	Al													
							0.412	253	27.2	0.446	(10.684)	(99.345)	0.340	Al													
							0.412	253	27.2	0.446	(10.684)	(99.345)	0.340	Al													
							0.412	253	27.2	0.446	(10.684)	(99.345)	0.340	Al													
							0.412	253	27.2	0.446	(10.684)	(99.345)	0.340	Al													
							0.412	253	27.2	0.446	(10.684)	(99.345)	0.340	Al													
							0.412	253	27.2	0.446	(10.684)	(99.345)	0.340	Al													
							0.412	253	27.2	0.446	(10.684)	(99.345)	0.340	Al													
							0.412	253	27.2	0.446	(10.684)	(99.345)	0.340	Al													
							0.412	253	27.2	0.446	(10.684)	(99.345)	0.340	Al													
							0.412	253	27.2	0.446	(10.684)	(99.345)	0.340	Al													
							0.412	253	27.2	0.446	(10.684)	(99.345)	0.340	Al													
							0.412	253	27.2	0.446	(10.684)	(99.345)	0.340	Al													
							0.412	253	27.2	0.446	(10.684)	(99.345)	0.340	Al													
							0.412	253	27.2	0.446	(10.684)	(99.345)	0.340	Al													
							0.412	253	27.2	0.446	(10.684)	(99.345)	0.340	Al													
							0.412	253	27.2	0.446	(10.684)	(99.345)	0.340	Al													
							0.412	253	27.2	0.446	(10.684)	(99.345)	0.340	Al													
							0.412	253	27.2	0.446	(10.684)	(99.345)	0.340	Al													
							0.412	253	27.2	0.446	(10.684)	(99.345)	0.340	Al													
							0.412	253	27.2	0.446	(10.684)	(99.345)	0.340	Al													
							0.412	253	27.2	0.446	(10.684)	(99.345)	0.340	Al													
							0.412	253	27.2	0.446	(10.684)	(99.345)	0.340	Al													
							0.412	253	27.2	0.446	(10.684)	(99.345)	0.340	Al													
							0.412	253	27.2	0.446	(10.684)	(99.345)	0.340	Al													
							0.412	253	27.2	0.446	(10.684)	(99.345)	0.340	Al													
							0.412	253	27.2	0.446	(10.684)	(99.345)	0.340	Al													
							0.412	253	27.2	0.446	(10.684)	(99.345)	0.340	Al													
							0.412	253	27.2	0.446	(10.684)	(99.345)	0.340	Al													
							0.412	253	27.2	0.446	(10.684)	(99.345)	0.340	Al													
							0.412	253	27.2	0.446	(10.684)	(99.345)	0.340	Al													
							0.412	253	27.2	0.446	(10.684)	(99.345)	0.340	Al													
							0.412	253	27.2	0.446	(10.684)	(99.345)	0.340	Al													
							0.412	253	27.2	0.446	(10.684)	(99.345)	0.340	Al													
							0.412	253	27.2	0.446	(10.684)	(99.345)	0.340	Al													
							0.412	253	27.2	0.446	(10.684)	(99.345)	0.340	Al													
							0.412	253	27.2	0.446	(10.684)	(99.345)	0.340	Al													
							0.412	253	27.2	0.446	(10.684)	(99.345)	0.340	Al													
							0.412	253	27.2	0.446	(10.684)	(99.345)	0.340	Al													
							0.412	253	27.2	0.446	(10.684)	(99.345)	0.340	Al													
							0.412	253	27.2	0.446	(10.684)	(99.345)	0.340	Al													
							0.412	253	27.2	0.446	(10.684)	(99.345)	0.340	Al													
							0.412	253	27.2	0.446	(10.684)	(99.345)	0.340	Al													
							0.412	253	27.2	0.446	(10.684)	(99.345)	0.340	Al													
							0.412	253	27.2	0.446	(10.684)	(99.345)	0.340	Al													
							0.412	253	27.2	0.446	(10.684)	(99.345)	0.340	Al													
							0.412	253	27.2	0.446	(10.684)	(99.345)	0.340	Al													
							0.412	253	27.2	0.446	(10.684)	(99.345)	0.340	Al													
							0.412	253	27.2	0.446	(10.684)	(99.345)	0.340	Al													
							0.412	253	27.2	0.446	(10.684)	(99.345)	0.340	Al													
							0.412	253	27.2	0.446	(10.684)	(99.345)	0.340	Al													
							0.412	253	27.2	0.446	(10.684)	(99.345)	0.340	Al													
							0.412	253	27.2	0.446	(10.684)	(99.345)	0.340	Al													
							0.412	253	27.2	0.446	(10.684)	(99.345)	0.340	Al													
							0.412	253	27.2	0.446	(10.684)	(99.345)	0.340	Al													
							0.412	253	27.2	0.446	(10.684)	(99.345)	0.340	Al													
							0.412	253	27.2	0.446	(10.684)	(99.345)	0.340	Al													
							0.412	253	27.2	0.446	(10.684)	(99.345)	0.340	Al													

( ) points in parentheses are less reliable

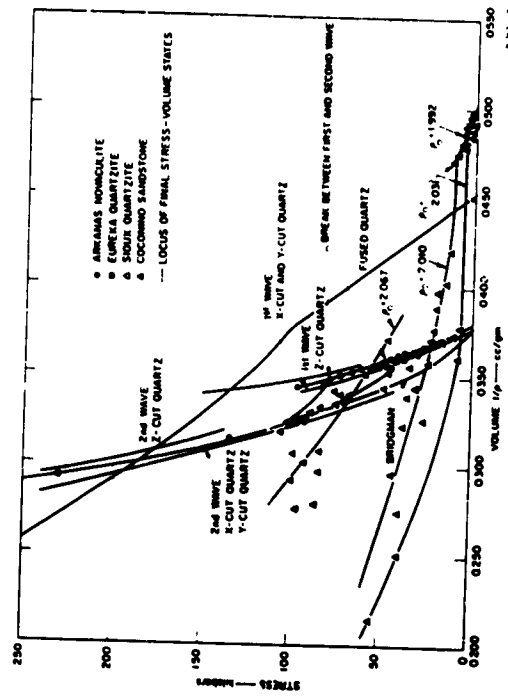


FIG. 18 HUGONIOTS FOR QUARTZ AND QUARTZ ROCKS

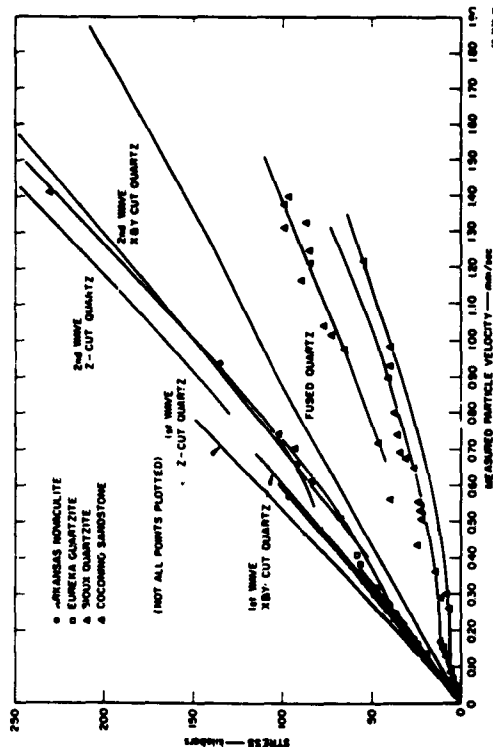


FIG. 19 STRESS vs. PARTICLE VELOCITY FOR QUARTZ ROCKS

From the data shown in Figs. 18 and 19 and from the observed differences and similarities of the rocks, the following conclusions are drawn:

1. In the main, Hugoniot data for the quartzites and novaculites agree with the single crystal data. That is, the velocities for the first waves agree and the velocity for the second wave lies between the velocities for the X, Y-cut and Z-cut quartz. The data for the sandstone scatters widely. This scatter occurs in the state of the second wave. Data from the first wave is more consistent but the peak stress and velocity is much less than in the single crystal.
2. The break in the stress-particle velocity graphs of the Arkansas novaculite, Sioux and Eureka quartzite, and Coconino sandstone indicates a transition from elastic to nonelastic behavior of the rock and not a phase transition. This is indicated by the wide range in transition pressures for the various rock types, although they are mineralogically the same. This is also shown by the agreement of the first wave velocities of the quartzites, and especially the novaculite, with those of the X-cut and Y-cut first-waves in crystal quartz.

No dynamic phase transitions in crystal quartz are reported at the temperatures and pressures obtained in these experiments. When a sample of novaculite, shocked to 100 kb, was recovered from one of our experiments and examined petrographically, no indication of a phase change was found in the inter-granular structure. However, coesite and stishovite are recorded in meteor craters and this indicates the possibility of finding them in the shock wave experiments at higher pressures. The break at about 400 kb in Wecherle's data is suggested by him to be a phase change to stishovite.

3. Porosity plays a major role in determining the velocity with which the first wave propagates. Fig. 20. Compare the propagation velocity of the first wave for novaculite, which has no porosity, with first wave velocity of other rocks (Table IV). The quartzites have less than 1 percent porosity and a first wave velocity slightly less than that of the novaculite; while the Coconino sandstone, with a porosity of about 23 percent, has a first wave velocity much less than the above rocks.
4. The peak stress amplitude of the first wave is dependent upon the porosity. Figure 21 shows that the peak stress is quite sensitive

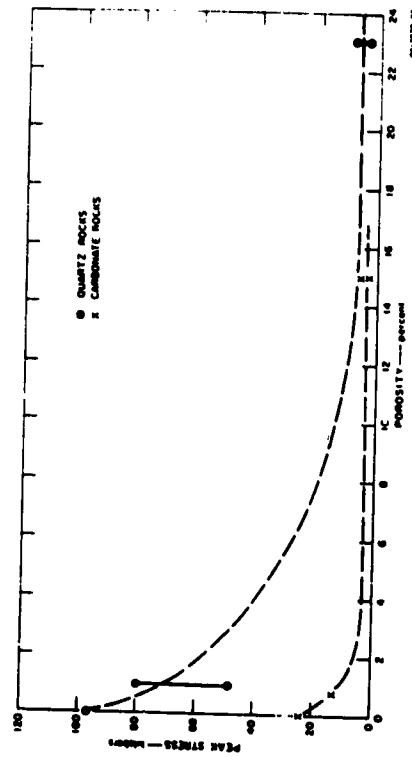


FIG. 21 PEAK STRESS OF FIRST WAVE vs. POROSITY FOR QUARTZ AND CARBONATE ROCKS

to porosity for the first few percent. It is possible that one of the parameters that controls porosity (e.g., cementation) plays a major role in the relationship. The secondary quartz overgrowths on the grains in the Sioux quartzite would influence the peak stress of the first wave if this were the case; unfortunately, the exact peak stress of the first wave from the Eureka quartzite is not available for comparison so that the proper importance of cementation can not be evaluated. It is expected that static compression tests will give a measure of the cementation effect.

Until more information is available, the peak stress amplitude will be assumed to be a function of porosity only.

5. The grain size of the rock has little influence on the shock wave parameters. There is no correlation of peak stress or first wave velocity with grain size. Besides which, for well sorted sand grains, the porosity does not depend upon grain size. The grain size may determine the rise time of the shock wave but no data are available to support the idea.

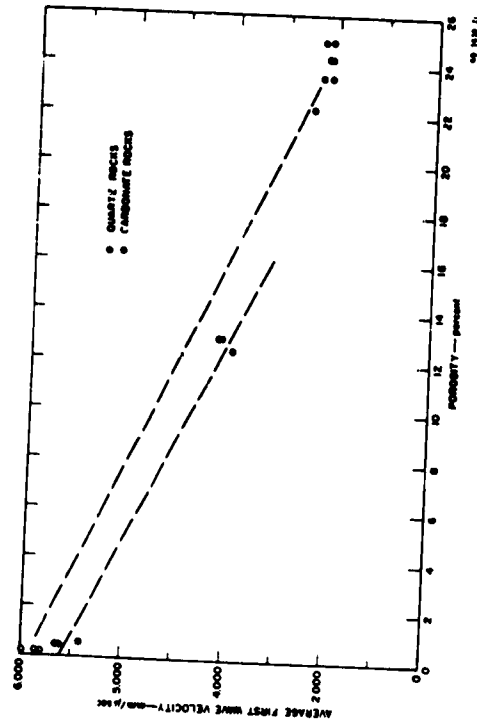


FIG. 20 AVERAGE FIRST WAVE VELOCITY vs. POROSITY FOR QUARTZ AND CARBONATE ROCKS



### C CALCITE

All the data obtained at SHI are recorded in Table III. The Plane-Wave Pellet Method was used in the experiments; others were performed but errors in the assemblies have devaluated the results. Further experiments are in progress. Figures 22, 23, and 24 include tentative graphs of the data for cleavage-cut calcite. It is uncertain whether the break between the two waves, 30 kb is a phase transition or an elastic to plastic transition. Adelerov, *et al.*,<sup>9</sup> have determined phase transitions in marble at 16, 21.5, 30 kb by static methods but, except for the transition at 30 kb which is in question, these transitions have not been detected by our dynamic measurements.

The second wave data in calcite lie to the right of the marble results. However, the scatter in the polycrystalline data is so large that it is difficult to say whether or not this effect is significant. Further work is required to clarify this point.

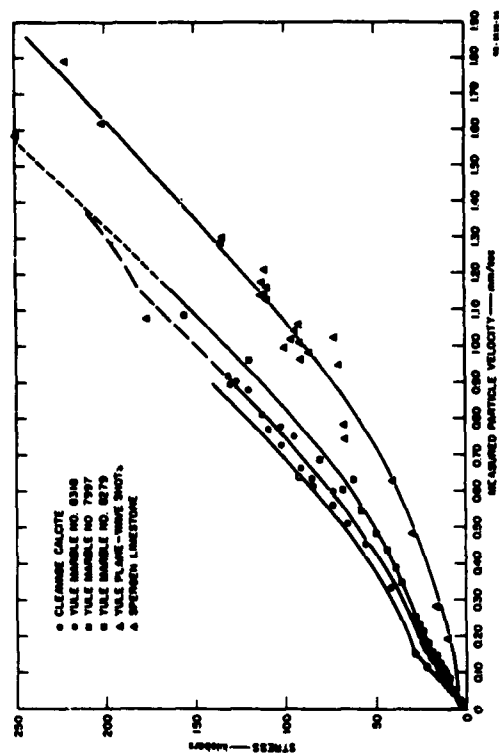


FIG. 22 STRESS vs. PARTICLE VELOCITY FOR CALCITE AND CARBONATE ROCKS

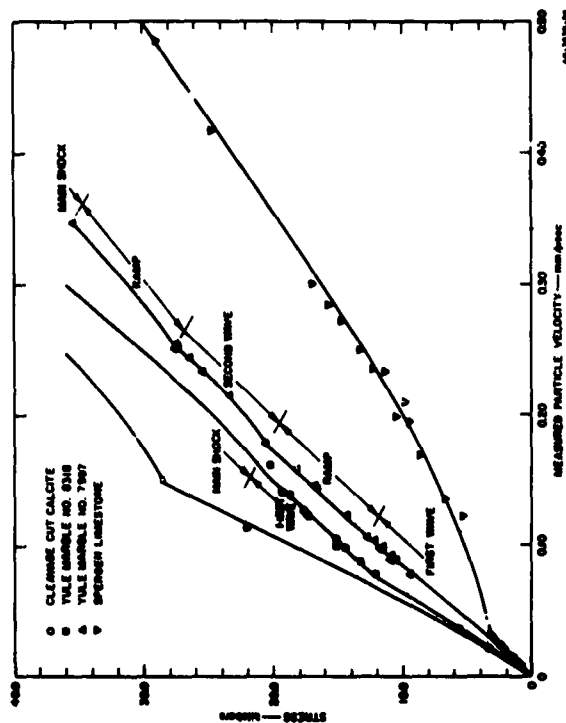


FIG. 23 STRESS vs. PARTICLE VELOCITY FOR CALCITE AND CARBONATE ROCKS

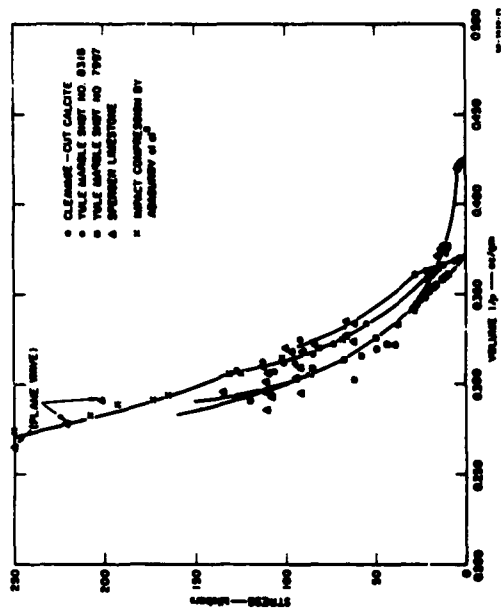


FIG. 24 HUGONIOT FOR CALCITE AND CARBONATE ROCKS

#### D. CARBONATE ROCKS

Table V and part of Table VI summarizes all the data for the carbonate rocks. Figures 22, 23, and 24 show plots of stress-particle velocity and stress-volume for Yule marble and Spargen limestone. Using the above data together with the differences and similarities of the rocks, the following conclusions are drawn:

1. For the carbonate rocks, agreement is poor among the Hugoniot data, Fig. 24. There are differences in the data between rock types as well as differences between the two-dimensional experiments and the plane-wave experiment on each rock. The general behavior is the same as in the quartz rocks, however. The velocities of the first waves in the carbonates is less than calcite; with the more porous rock having the lowest first wave velocity.

Table V  
SUMMARY OF DATA FOR CARBONATE ROCKS, TWO-DIMENSIONAL WEDGE EXPERIMENTS

ROCK PARAMETERS										WEDGE PARAMETERS									
Shot No.	Section Name	Distance Velocity (in./sec.)	Explosive Type	Thick-wave (in.)	Section Density (g/cm <sup>3</sup> )	Depth in Shot (in.)	Shot Angle (deg.)	Shot Velocity (in./sec.)	Particle Velocity (in./sec.)	Ratio $P_p/P_s$	Strain (in.)	Volume (cc/g)	Wave	Notes					
Tule Marble	8218	A = 26.6 B = 5.1 C = 9.1	Comp B	1.0	2.693	1.46	47.0	15,000	0.000	0.000	0.000	0.000	1	First wave	1				
						1.46	48.3	15,000	0.000	0.000	0.000	0.000	2	Second wave	2				
						1.46	49.6	15,000	0.000	0.000	0.000	0.000	3	Third wave	3				
						1.46	50.9	15,000	0.000	0.000	0.000	0.000	4	Fourth wave	4				
						1.46	52.2	15,000	0.000	0.000	0.000	0.000	5	Fifth wave	5				
						1.46	53.5	15,000	0.000	0.000	0.000	0.000	6	Sixth wave	6				
						1.46	54.8	15,000	0.000	0.000	0.000	0.000	7	Seventh wave	7				
						1.46	56.1	15,000	0.000	0.000	0.000	0.000	8	Eighth wave	8				
						1.46	57.4	15,000	0.000	0.000	0.000	0.000	9	Ninth wave	9				
						1.46	58.7	15,000	0.000	0.000	0.000	0.000	10	Tenth wave	10				
						1.46	60.0	15,000	0.000	0.000	0.000	0.000	11	Eleventh wave	11				
						1.46	61.3	15,000	0.000	0.000	0.000	0.000	12	Twelfth wave	12				
						1.46	62.6	15,000	0.000	0.000	0.000	0.000	13	Thirteenth wave	13				
						1.46	63.9	15,000	0.000	0.000	0.000	0.000	14	Fourteenth wave	14				
						1.46	65.2	15,000	0.000	0.000	0.000	0.000	15	Fifteenth wave	15				
						1.46	66.5	15,000	0.000	0.000	0.000	0.000	16	Sixteenth wave	16				
						1.46	67.8	15,000	0.000	0.000	0.000	0.000	17	Seventeenth wave	17				
						1.46	69.1	15,000	0.000	0.000	0.000	0.000	18	Eighteenth wave	18				
						1.46	70.4	15,000	0.000	0.000	0.000	0.000	19	Nineteenth wave	19				
						1.46	71.7	15,000	0.000	0.000	0.000	0.000	20	Twentieth wave	20				

( ) values in parentheses are less reliable



Table V Continued

Shot	Shot No.	BASIC PARAMETERS			SHOCK PARAMETERS										Waveform	Mirror	Notes
		Specimen Dimensions	Distance	Explosive	Depth	Shot Angle	Shot Velocity	Particle Velocity	$\rho_0/\rho$	Stress	Volume						
		A = 11.5" x 11.5" x 11.5" B = 4" x 4" x 4" C = 10.1"	7.874	Camp B	2.720	32.5°	3.200	0.097	0.976	11.419	0.10						
						32.5°	3.200	0.104	0.975	12.163	0.10						
						32.5°	3.200	0.110	0.974	12.908	0.10						
						32.5°	3.200	0.116	0.973	13.653	0.10						
						32.5°	3.200	0.122	0.972	14.398	0.10						
						32.5°	3.200	0.128	0.971	15.143	0.10						
						32.5°	3.200	0.134	0.970	15.888	0.10						
						32.5°	3.200	0.140	0.969	16.633	0.10						
						32.5°	3.200	0.146	0.968	17.378	0.10						
						32.5°	3.200	0.152	0.967	18.123	0.10						
						32.5°	3.200	0.158	0.966	18.868	0.10						
						32.5°	3.200	0.164	0.965	19.613	0.10						
						32.5°	3.200	0.170	0.964	20.358	0.10						
						32.5°	3.200	0.176	0.963	21.103	0.10						
						32.5°	3.200	0.182	0.962	21.848	0.10						
						32.5°	3.200	0.188	0.961	22.593	0.10						
						32.5°	3.200	0.194	0.960	23.338	0.10						
						32.5°	3.200	0.200	0.959	24.083	0.10						
						32.5°	3.200	0.206	0.958	24.828	0.10						
						32.5°	3.200	0.212	0.957	25.573	0.10						
						32.5°	3.200	0.218	0.956	26.318	0.10						
						32.5°	3.200	0.224	0.955	27.063	0.10						
						32.5°	3.200	0.230	0.954	27.808	0.10						
						32.5°	3.200	0.236	0.953	28.553	0.10						
						32.5°	3.200	0.242	0.952	29.298	0.10						
						32.5°	3.200	0.248	0.951	30.043	0.10						
						32.5°	3.200	0.254	0.950	30.788	0.10						
						32.5°	3.200	0.260	0.949	31.533	0.10						
						32.5°	3.200	0.266	0.948	32.278	0.10						
						32.5°	3.200	0.272	0.947	33.023	0.10						
						32.5°	3.200	0.278	0.946	33.768	0.10						
						32.5°	3.200	0.284	0.945	34.513	0.10						
						32.5°	3.200	0.290	0.944	35.258	0.10						
						32.5°	3.200	0.296	0.943	36.003	0.10						
						32.5°	3.200	0.302	0.942	36.748	0.10						
						32.5°	3.200	0.308	0.941	37.493	0.10						
						32.5°	3.200	0.314	0.940	38.238	0.10						
						32.5°	3.200	0.320	0.939	38.983	0.10						
						32.5°	3.200	0.326	0.938	39.728	0.10						
						32.5°	3.200	0.332	0.937	40.473	0.10						
						32.5°	3.200	0.338	0.936	41.218	0.10						
						32.5°	3.200	0.344	0.935	41.963	0.10						
						32.5°	3.200	0.350	0.934	42.708	0.10						
						32.5°	3.200	0.356	0.933	43.453	0.10						
						32.5°	3.200	0.362	0.932	44.198	0.10						
						32.5°	3.200	0.368	0.931	44.943	0.10						
						32.5°	3.200	0.374	0.930	45.688	0.10						
						32.5°	3.200	0.380	0.929	46.433	0.10						
						32.5°	3.200	0.386	0.928	47.178	0.10						
						32.5°	3.200	0.392	0.927	47.923	0.10						
						32.5°	3.200	0.398	0.926	48.668	0.10						
						32.5°	3.200	0.404	0.925	49.413	0.10						
						32.5°	3.200	0.410	0.924	50.158	0.10						
						32.5°	3.200	0.416	0.923	50.903	0.10						
						32.5°	3.200	0.422	0.922	51.648	0.10						
						32.5°	3.200	0.428	0.921	52.393	0.10						
						32.5°	3.200	0.434	0.920	53.138	0.10						
						32.5°	3.200	0.440	0.919	53.883	0.10						
						32.5°	3.200	0.446	0.918	54.628	0.10						
						32.5°	3.200	0.452	0.917	55.373	0.10						
						32.5°	3.200	0.458	0.916	56.118	0.10						
						32.5°	3.200	0.464	0.915	56.863	0.10						
						32.5°	3.200	0.470	0.914	57.608	0.10						
						32.5°	3.200	0.476	0.913	58.353	0.10						
						32.5°	3.200	0.482	0.912	59.098	0.10						
						32.5°	3.200	0.488	0.911	59.843	0.10						
						32.5°	3.200	0.494	0.910	60.588	0.10						
						32.5°	3.200	0.500	0.909	61.333	0.10						
						32.5°	3.200	0.506	0.908	62.078	0.10						
						32.5°	3.200	0.512	0.907	62.823	0.10						
						32.5°	3.200	0.518	0.906	63.568	0.10						
						32.5°	3.200	0.524	0.905	64.313	0.10						
						32.5°	3.200	0.530	0.904	65.058	0.10						
						32.5°	3.200	0.536	0.903	65.803	0.10						
						32.5°	3.200	0.542	0.902	66.548	0.10						
						32.5°	3.200	0.548	0.901	67.293	0.10						
						32.5°	3.200	0.554	0.900	68.038	0.10						
						32.5°	3.200	0.560	0.899	68.783	0.10						
						32.5°	3.200	0.566	0.898	69.528	0.10						
						32.5°	3.200	0.572	0.897	70.273	0.10						
						32.5°	3.200	0.578	0.896	71.018	0.10						
						32.5°	3.200	0.584	0.895	71.763	0.10						
						32.5°	3.200	0.590	0.894	72.508	0.10						
						32.5°	3.200	0.596	0.893	73.253	0.10						
						32.5°	3.200	0.602	0.892	74.000	0.10						
						32.5°	3.200	0.608	0.891	74.745	0.10						
						32.5°	3.200	0.614	0.890	75.490	0.10						
						32.5°	3.200	0.620	0.889	76.235	0.10						
						32.5°	3.200	0.626	0.888	76.980	0.10						
						32.5°	3.200	0.632	0.887	77.725	0.10						
						32.5°	3.200	0.638	0.886	78.470	0.10						
						32.5°	3.200	0.644	0.885	79.215	0.10						
						32.5°	3.200	0.650	0.884	79.960	0.10						
						32.5°	3.200	0.656	0.883	80.705	0.10						
						32.5°	3.200	0.662	0.882	81.450	0.10						
						32.5°	3.200	0.668	0.881	82.195	0.10						
						32.5°	3.200	0.674	0.880	82.940	0.10						
						32.5°	3.200	0.680	0.879	83.685	0.10						
						32.5°	3.200	0.686	0.878	84.430	0.10						
						32.5°	3.200	0.692	0.877	85.175	0.10						
						32.5°	3.200	0.698	0.876	85.920	0.10						
						32.5°	3.200	0.704	0.875	86.665	0.10						
						32.5°	3.200	0.710	0.874	87.410	0.10						
						32.5°	3.200	0.716	0.873	88.155	0.10						
						32.5°	3.200	0.722	0.872	88.900	0.10						
						32.5°	3.200	0.728	0.871	89.645	0.10						
						32.5°	3.200	0.734	0.870	90.390	0.10						
						32.5°	3.200	0.740	0.869	91.135	0.10						

Table V Continued

SWISS PARAMETERS												BOLZ PARAMETERS											
Rock	Shot No.	Specimen Dimensions	Detonation Velocity (m/sec)	Explosive Type	Thickness (in.)	Specimen Density (g/cc)	Depth in Rock (in.)	Shank Angle (deg)	Shank Velocity (cm/sec)	Particle Velocity (cm/sec)	Ratio $P_p/P_s$	Strain (in.)	Volume (cc/g)	Mirror	Notes								
Talc Marble	7997 (Cont)	A = 41.75 b = 2.8 c = 10.1	7,874	Comp B	0.25	2.728	1.217	23.3	3.43	0.143	0.062	15.173	0.354	0.354	A	Thick wave							
							1.411	23.9	3.49	0.146	0.062	15.770	0.375	0.375	A	Thick wave							
							1.413	24.0	3.50	0.146	0.062	15.770	0.375	0.375	A	Thick wave							
							1.413	24.0	3.50	0.146	0.062	15.770	0.375	0.375	A	Thick wave							
							1.413	24.0	3.50	0.146	0.062	15.770	0.375	0.375	A	Thick wave							
							1.413	24.0	3.50	0.146	0.062	15.770	0.375	0.375	A	Thick wave							
							1.413	24.0	3.50	0.146	0.062	15.770	0.375	0.375	A	Thick wave							
							1.413	24.0	3.50	0.146	0.062	15.770	0.375	0.375	A	Thick wave							
							1.413	24.0	3.50	0.146	0.062	15.770	0.375	0.375	A	Thick wave							
							1.413	24.0	3.50	0.146	0.062	15.770	0.375	0.375	A	Thick wave							
Spergon Limestone	8118	A = 31.1 b = 3.0 c = 11.8	7,940	Comp B	0.25	2.394	0.977	19.2	2.42	0.118	0.037	19.905	0.408	0.408	A	First wave							
							1.201	17.6	2.62	0.118	0.037	19.905	0.408	0.408	A	First wave							
							1.441	14.5	1.97	0.093	0.035	19.905	0.408	0.408	A	First wave							
							1.552	14.5	1.97	0.093	0.035	19.905	0.408	0.408	A	First wave							
							1.729	20.5	2.791	0.137	0.053	19.905	0.408	0.408	A	First wave							
							1.729	18.2	2.480	0.135	0.053	19.905	0.408	0.408	A	First wave							
							1.729	16.2	2.215	0.134	0.054	19.905	0.408	0.408	A	First wave							
							1.729	14.6	2.038	0.136	0.054	19.905	0.408	0.408	A	First wave							
							1.729	12.3	1.754	0.139	0.054	19.905	0.408	0.408	A	First wave							
							1.729	10.3	1.507	0.140	0.054	19.905	0.408	0.408	A	First wave							
Spergon Limestone	8162	A = 28.0 b = 3.0 c = 11.9	7,850	Comp B	0.25	2.340	0.944	16.7	2.54	0.109	0.035	19.905	0.408	0.408	A	First wave							
							1.218	16.1	2.416	0.109	0.035	19.905	0.408	0.408	A	First wave							
							1.399	16.1	2.416	0.109	0.035	19.905	0.408	0.408	A	First wave							
							1.514	16.1	2.416	0.109	0.035	19.905	0.408	0.408	A	First wave							
							1.640	16.1	2.416	0.109	0.035	19.905	0.408	0.408	A	First wave							
							1.718	16.1	2.416	0.109	0.035	19.905	0.408	0.408	A	First wave							
							1.718	16.1	2.416	0.109	0.035	19.905	0.408	0.408	A	First wave							
							1.718	16.1	2.416	0.109	0.035	19.905	0.408	0.408	A	First wave							
							1.718	16.1	2.416	0.109	0.035	19.905	0.408	0.408	A	First wave							
							1.718	16.1	2.416	0.109	0.035	19.905	0.408	0.408	A	First wave							

( ) points in parentheses are less reliable.

Table V Continued

Rock	SECE PARAMETERS				SECE PARAMETERS							Notes
	Shot No.	Specimen Name	Specimen Weight (lb.)	Explosive Type	Shot Size (mm)	Shot Angle (deg)	Shot Velocity (cm/sec)	Shot Velocity (ft/sec)	Shot Velocity (in./sec)	Shot Velocity (mm/sec)	Shot Velocity (cm/sec)	Shot Velocity (ft/sec)
Spergen Limestone	8142 (Cont.)	A = 20.4 B = 3.0 C = 11.5	2.300	Comp B	7.000	1.000	4.175	10.000	10.000	10.000	10.000	10.000
						1.000	4.175	10.000	10.000	10.000	10.000	10.000
						1.000	4.175	10.000	10.000	10.000	10.000	10.000
						1.000	4.175	10.000	10.000	10.000	10.000	10.000
						1.000	4.175	10.000	10.000	10.000	10.000	10.000
						1.000	4.175	10.000	10.000	10.000	10.000	10.000
						1.000	4.175	10.000	10.000	10.000	10.000	10.000
						1.000	4.175	10.000	10.000	10.000	10.000	10.000
						1.000	4.175	10.000	10.000	10.000	10.000	10.000
						1.000	4.175	10.000	10.000	10.000	10.000	10.000
						1.000	4.175	10.000	10.000	10.000	10.000	10.000
						1.000	4.175	10.000	10.000	10.000	10.000	10.000
						1.000	4.175	10.000	10.000	10.000	10.000	10.000
						1.000	4.175	10.000	10.000	10.000	10.000	10.000
						1.000	4.175	10.000	10.000	10.000	10.000	10.000
						1.000	4.175	10.000	10.000	10.000	10.000	10.000
						1.000	4.175	10.000	10.000	10.000	10.000	10.000
						1.000	4.175	10.000	10.000	10.000	10.000	10.000
						1.000	4.175	10.000	10.000	10.000	10.000	10.000
						1.000	4.175	10.000	10.000	10.000	10.000	10.000
						1.000	4.175	10.000	10.000	10.000	10.000	10.000
Spergen Limestone	8552	A = 20.4 B = 3.0 C = 11.5	2.300	Comp B	7.000	1.000	4.175	10.000	10.000	10.000	10.000	10.000
						1.000	4.175	10.000	10.000	10.000	10.000	10.000

( ) values in parentheses are less reliable.

Table V Continued

Rock	BICE PARAMETERS				BICE PARAMETERS							Notes
	Shot No.	Specimen Dimensions (in.)	Specimen Weight (lb.)	Explosive Type	Shot Velocity (ft/sec)	Shot Angle (deg)	Shot Velocity (ft/sec)	Shot Velocity (ft/sec)	Shot Velocity (ft/sec)	Shot Velocity (ft/sec)	Shot Velocity (ft/sec)	
Spartan Limestone	6523	A = 2.0 B = 1.0 C = 1.0	7.993	Comp B	2.381	0.00	0.00	0.00	0.00	0.00	0.00	Pressure not readable at this position
							0.00	0.00	0.00	0.00	0.00	
							0.00	0.00	0.00	0.00	0.00	
							0.00	0.00	0.00	0.00	0.00	
							0.00	0.00	0.00	0.00	0.00	
							0.00	0.00	0.00	0.00	0.00	
							0.00	0.00	0.00	0.00	0.00	
							0.00	0.00	0.00	0.00	0.00	
							0.00	0.00	0.00	0.00	0.00	
							0.00	0.00	0.00	0.00	0.00	
Spartan Limestone	6524	A = 2.0 B = 1.0 C = 1.0	7.225	Comp B	2.381	0.00	0.00	0.00	0.00	0.00	0.00	First wave
							0.00	0.00	0.00	0.00	0.00	
							0.00	0.00	0.00	0.00	0.00	
							0.00	0.00	0.00	0.00	0.00	
							0.00	0.00	0.00	0.00	0.00	
							0.00	0.00	0.00	0.00	0.00	
							0.00	0.00	0.00	0.00	0.00	
							0.00	0.00	0.00	0.00	0.00	
							0.00	0.00	0.00	0.00	0.00	
							0.00	0.00	0.00	0.00	0.00	

( ) points in parentheses are less reliable.



Table VI  
SUMMARY OF DATA FOR PLANE WAVE SHOTS

ROCK	IDENT. NO.	COMMENT	EXPOSURE P-40	ALUMINUM			ROCK			NOTES			
				Free-Surface Velocity (m/sec)	Shock Velocity (m/sec)	Stress (ksi)	Free-Surface Velocity (m/sec)	Shock Velocity (m/sec)	Particle Velocity (m/sec)	Stress (ksi)	Ratio (v <sub>s</sub> /v <sub>f</sub> )	Shear (kg/cm <sup>2</sup> )	Volume (cc/g)
Aluminum-Normalite	8230	Plane-wave horizontal pellet	none	1.188	..	103	1.064	5.88	0.660	42.6	0.0096	2.48	0.315
	8270	Plane-wave horizontal pellet	none	1.085	..	131	1.143	3.18	0.660	96.7	0.0096	2.48	0.315
	8272	Plane-wave horizontal pellet	2-Camp B	1.085	..	131	1.143	3.18	0.940	135	0.036	2.48	0.316
	8273	Plane-wave horizontal pellet	2-Camp B	1.085	..	131	1.143	3.18	0.940	135	0.036	2.48	0.316
Silica Quartzite	7635	Plane-wave horizontal pellet	none	1.178	..	102	1.064	6.30	0.660	233	0.0096	2.48	0.292
	8123	Plane-wave horizontal pellet	none	1.178	..	102	1.064	6.30	0.660	233	0.0096	2.48	0.292
	7642	Plane-wave horizontal pellet	none	1.178	..	102	1.064	6.30	0.660	233	0.0096	2.48	0.292
	7713	Plane-wave horizontal pellet	1-Camp B	1.178	..	102	1.064	6.30	0.660	233	0.0096	2.48	0.292
Talc Marble	8231	Plane-wave horizontal pellet	none	1.178	..	102	1.064	6.30	0.660	233	0.0096	2.48	0.292
	8232	Plane-wave horizontal pellet	none	1.178	..	102	1.064	6.30	0.660	233	0.0096	2.48	0.292
	8233	Plane-wave horizontal pellet	none	1.178	..	102	1.064	6.30	0.660	233	0.0096	2.48	0.292
	8234	Plane-wave horizontal pellet	none	1.178	..	102	1.064	6.30	0.660	233	0.0096	2.48	0.292
Spergon Limestone	8150	Plane-wave horizontal pellet	none	1.161	..	100	1.064	6.30	0.660	233	0.0096	2.48	0.292
	8151	Plane-wave horizontal pellet	none	1.161	..	100	1.064	6.30	0.660	233	0.0096	2.48	0.292
	8152	Plane-wave horizontal pellet	none	1.161	..	100	1.064	6.30	0.660	233	0.0096	2.48	0.292
	8153	Plane-wave horizontal pellet	none	1.161	..	100	1.064	6.30	0.660	233	0.0096	2.48	0.292

\* Inclined mirror measurement  
( ) points in parentheses are less reliable  
§ Free free-surface velocity in aluminum, curved wave arrival time 7.87.

80

There is one area of agreement. Data from the two-dimensional shot, 8318, and plane-wave shots on marble and limestone agree with data by Adadurov, et al. (Figs. 25 and 26).

2. There is evidence for both yield and phase transitions in the carbonates. All of the data records at least one break in the stress-particle velocity curve with two breaks occurring for one marble and one limestone experiment. The first break is recorded at 28 kilobars in calcite, 21 and 12 kilobars in marble, and 3 kilobars in limestone. This indicates that the first break is a yield transition that may sometimes be influenced by phase transitions. The second break occurs at

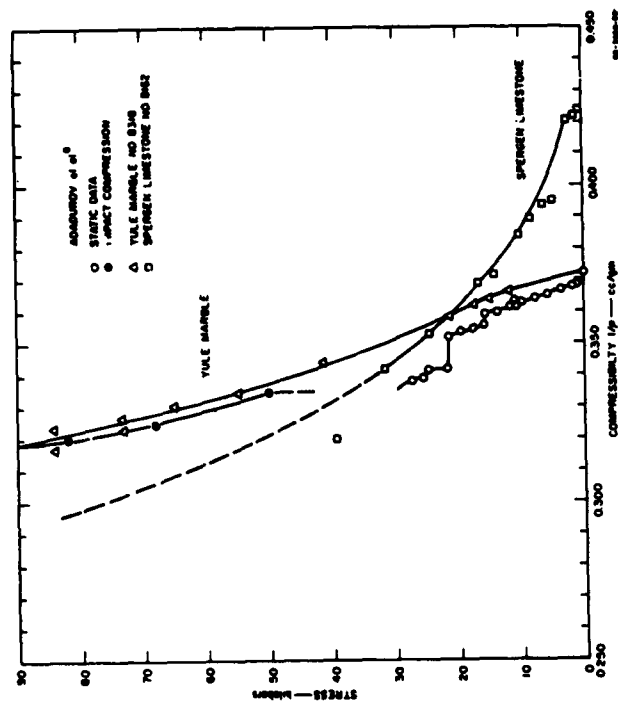


FIG. 25 HUGONIOT FOR CARBONATE ROCKS

about 30 kilobars (data from the limestone experiment is less reliable) and is probably a phase transition. The phase transition reported at 150 kilobars by Adadurov, et al. is also indicated in the above experiments by a 'break' in the Hugoniot curve at about 150 kilobars.

Additional evidence for yield is found in some of the recovered samples of Yule marble. The stress produced in the sample was 100 kilobars or less and an examination of thin sections from the sample showed that the number of twin planes in the individual crystals doubled. This yield mechanism in calcite is not completely understood in detail but has been studied extensively by Turner, et al.

3. Porosity plays a major role in determining the velocity with which the first wave propagates. Fig. 20. The propagation velocity of the first wave in the marble, porosity 0.75 percent, is greater than the velocity of the first wave in limestone, porosity 15 percent.

4. The peak stress amplitude of the first wave is dependent upon the porosity. Figure 21 shows that the peak stress is quite sensitive to porosity for the first few percent. It is possible that one of the parameters that controls porosity plays a major role in the relationship but it is uncertain which one. The porosity in the marble and limestone is primarily the result of chemical processes involved in metamorphism and diagenesis and has little relation to the original porosity of the rock. Relationships of porosity to other rock parameters in this situation are not understood as well as in the quartz rocks.

Until more information is available, the peak stress amplitude will be assumed to be a function of porosity only.

5. The grain size of the rock has little influence on the shock wave parameters. There is no correlation of the peak stress or first wave velocity with grain size. The grain size may determine the rise time of the shock wave but no data are available to support this idea.

A comparison between Shot 7997 and 8318 in Yule marble makes the discussion above somewhat uncertain. The problem is that 8318 is a shot in which the C-axis of the calcite grains were parallel to the ray path of the detonation front; Shot 7997 was not, but the exact orientation is not known. Since the sound velocity is slower along the C-axis in calcite, the first wave velocity in 8318 should be less than that in 7997. It is not, however, and the reason for the discrepancy is not understood. Shot 8279 covered such a small pressure range that it is neglected on some of the figures.

## PETROGRAPHIC DESCRIPTIONS

## APPENDIX A

## PETROGRAPHIC DESCRIPTIONS

The following rocks were used in the experiments.

## ARKANSAS NOVACULITE

Arkansas novaculite is a formation name for a novaculite-shale sequence of Devonian age and also a trade name. The formation is found in southwestern Arkansas and southeastern Oklahoma.

The Arkansas novaculite is a white to gray-white, microcrystalline quartz rock composed of 100 percent quartz grains. Sometimes differences in color and banding are present indicating a possible layering.

The average grain size is 0.01 mm in diameter with occasional grains 0.05 mm in diameter. The surfaces of the individual grains have a curved appearance characteristic of the novaculite-type rocks.<sup>11</sup> A powder X-ray diffraction pattern was made (Fig. 26) from a sample of the rock and was identical with a pattern made from alpha-quartz. The orientation of the grains is assumed to be random. This has almost always been the case from X-ray diffraction analysis.<sup>11</sup>

No porosity was observed in a thin section. The density of the novaculite is 2.649 g/cc. This also adds evidence that the rock is a pure quartz rock with at most a porosity of a few tenths of a percent if there is no water included in the rock. Some novaculite contains included water. If so, the amount of water will determine the decrease in density from that of pure quartz, 2.653 g/cc. The rock is well cemented. No quartz overgrowths or pore filling was detected.

Some of the novaculite was recovered from one of the experiments in which pressures of less than 100 kilobars were generated. A study of the thin section shows no observable difference from material studied before the experiment.

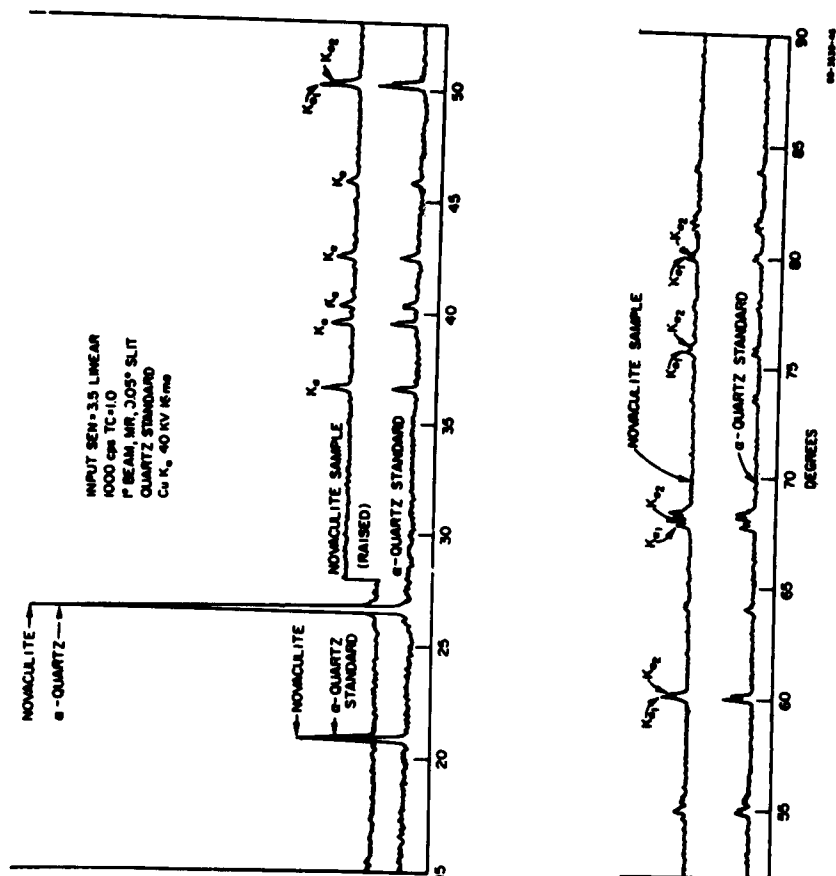


FIG. 26 X-RAY DIFFRACTION PATTERN OF ARKANSAS NOVACULITE

# COCOMINO SANDSTONE

This formation is in the Aubrey group and is Permian in age. The sandstone is found in northern Arizona, southern Utah, and southeastern Nevada.

The following description is taken from a personal communication from H. J. Moore<sup>1</sup> and agrees with the results from samples that were used in this series of experiments.

The Cocomino sandstone "is a laminated, yellowish gray, weakly cemented, fine-grained sandstone composed of about 97 percent quartz, 3 percent feldspar" (microcline and orthoclase), "and a fraction of 2 percent of clay and heavy minerals."

"Average and modal grain size of the sandstone is between 0.117 and 0.145 mm in diameter; the grains," which are sub-rounded, "range from less than 0.062 to 0.71 mm across." Subparallel laminae 5.0 to 17.5 mm thick are separated by thin laminae 0.5 mm thick containing more than average amounts of silt and clay-sized grains. The bulk density, measured from rectangular-sized blocks, is 2.26 g/cc; "but ranges to 2.06 g/cc; "the grain density is 2.67 g/cc, and the calculated porosity is 15 to 25 percent. The sandstone is only weakly to moderately well cemented with silica, mainly in the form of quartz overgrowths on the sand grains." (About 20 percent of the quartz grains have the overgrowths. The individual overgrowth has a different optic orientation than the grain itself.) "Some laminae can be disaggregated with finger pressure. Unconfined crushing strengths measure, perpendicular to the bedding of three 2.2 cm by 2.2 cm by 5 cm blocks under load applied in the long direction were 320 and 371 kg/cm<sup>2</sup> for water free specimens."

The plot of the c-axis of quartz grains (Fig. 27) shows that the axes are primarily parallel to the plane of the bedding and are grouped in either of two directions.

Using the classification of pure sandstones (Fig. 28) by Gilbert,<sup>13</sup> the Cocomino sandstone can be considered as an "end member" and would be termed a quartz arenite.



## EUREKA QUARTZITE

This formation is middle Ordovician in age and is found in northern Nevada, western Utah, and Inyo county, California.

The Eureka quartzite is a massive, white, fine grained, quartzite composed of about 98 percent quartz, and a percent or two of orthoclase feldspar.

The grain size ranges from 0.05 mm to 0.5 mm and the average grain size is 0.1 mm to 0.2 mm in diameter. The grains are sub-angular. The rock is strongly cemented by pore fillings and grain contacts. No secondary quartz overgrowths were present. The quartzite contains occasional fractures that are cemented with silica.

The porosity is less than 1 percent.

The plot of the c-axis of the quartz grains (Fig. 29) shows that the c-axes lie in two broad bands. This is probably a relic bedding rather than a result of any metamorphism. The degree of mineral alignment in the quartzite did not seem to affect the results of the experiments with the rock.

The quartzite can be considered an "end member" and would be called an orthoquartzite.

## SPIRGEN LIMESTONE

Indiana limestone or Indiana marble is the trade name for the Spargen limestone. This formation belongs to the Meramec group, is Mississippian in age and is found in southern Indiana. The formation was called the Bedford limestone but is now termed the Spargen limestone by U.S. Geological Survey. The Indiana and Illinois Geological Surveys use the term Salem limestone.

The Spargen limestone is a gray, well cemented, microcoquina composed of about 60 percent fossil fragments, 20 percent bioclastic debris including carbonate detritus, 20 percent calcite and a percent or two of oolites. The fossil debris is composed primarily of bryozoan fragments together with complete tests of Foraminifera (Endothyra). Some brachiopod and crinoid fragments are also present.

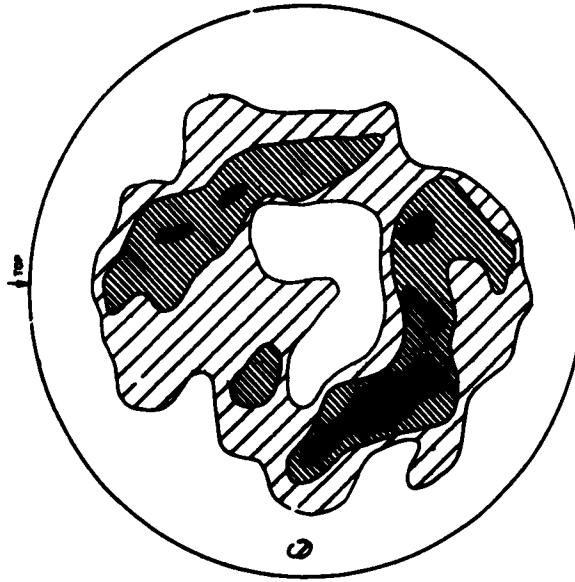


FIG. 29 FABRIC ORIENTATION OF EUREKA QUARTZITE

The size of the sub-rounded fragments range from 0.1 mm to 0.7 mm with the average size being about 0.3 to 0.4 mm in diameter. The average grain size of the void filling calcite is 0.2 to 0.3 mm in diameter with an occasional grain as large as 1.0 mm in diameter.

The calcite grains tend to have a "sub-poikiloblastic" texture. Some of the bioclastic fragments, which are included in the grains of cementing calcite have the same optic orientation as the neighboring calcite grains.

The porosity is about 12 percent. The density ranges from 2.360 to 2.398 g/cc.

The plot of the c-axis of the calcite grains and fossil detritus shows that there is no marked anisotropy of the fabric (Fig. 30).

According to the classification by Pettijohn,<sup>14</sup> the rock would be an "end member" and called an encrinite or microcoquina (Fig. 31).

#### SIoux QUARTZITE

The Sioux quartzite is Pre-Cambrian and is found in southeastern South Dakota, southwestern Minnesota, northwestern Iowa, and northeastern Nebraska.

The Sioux quartzite is a reddish, massive rock with no indication of bedding. The rock is composed of 99 percent quartz and less than one percent of clinozoisite and tourmaline. The clinozoisite and tourmaline are inclusions in the individual quartz grains. About 3 percent of the grains are composed of a fine-grained quartz.

The rounded grains range in size from 0.1 mm to 1.0 mm and the average size is 0.6 mm. The rounded grains have a quartz overgrowth. The rounded grains are outlined by a fine hematite dust between the grain and the overgrowth.

The porosity is less than 1 percent. The rock is strongly cemented by the quartz overgrowths.

The rock fabric was not studied.

The rock would be termed an orthoquartzite.

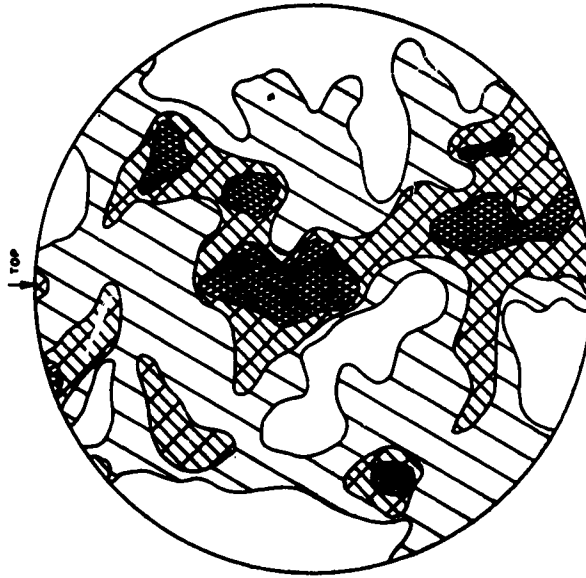


FIG. 30 FABRIC ORIENTATION OF SPARGEN LIMESTONE

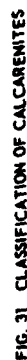
The Yule marble is a trade name for the marble quarried from the metamorphosed Leadville limestone in Gunnison county, Colorado. The Leadville limestone is Mississippian in age.

The average grain size of the marble is between 0.2 mm and 0.4 mm with an occasional grain as large as 1.5 mm in diameter (apparent grain size in the thin section depends upon orientation as the grains are platy).

Some samples were recovered from an experiment in which the pieces probably were at shock pressures of less than 50 kilobars. A study of the thin sections shows that there is an increase in the number of twin lamellae and that the twin lamellae seem to be at a different spacing than before the experiment. The distance between the twin lamellae increased from the shock pressure is much less than the distance between many of the lamellae in samples before the experiments. An approximate number of twins per grain before the experiment is about 3 with a range of 0 to 5. An approximate number of twins per grain after the experiment is about 7 with a range of 4 to 10.

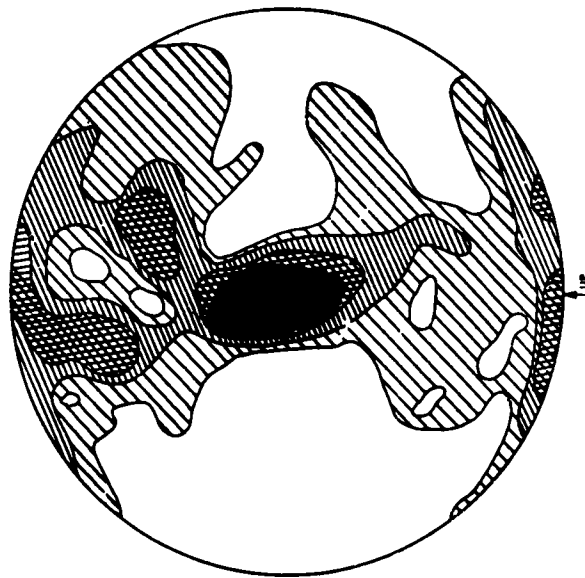
All descriptions of the rocks were obtained by observing hand specimens and studying orientated thin sections under the petrographic microscope. The accuracy of the points used in constructing the equal area projections is 5 percent and occasional checks were made by repeating observations. The study of the mineral orientation of the rocks had a twofold purpose:

1. The presence and the degree of mineral orientation in the samples might affect the interpretation of the results.
2. Once the direction of mineral alignment is known, the specimens used in the experiments can be oriented to determine the effect of the mineral alignment.





APPENDIX B  
SAMPLE TESTING AND PREPARATION



NOTE  
PLOT OF 302 C-AXIS OF CALCITE GRAINS IN THE YULE MARBLE  
CONTOURS ARE 1, 2, 3, 5 PERCENT PER ONE PERCENT AREA

FIG. 32 FABRIC ORIENTATION OF YULE MARBLE

## APPENDIX B

### SAMPLE TESTING AND PREPARATION

#### BULK DENSITY

A sample from each rock was cut into a parallelepiped with a rotary diamond saw. The sample was then baked at 120°C until its weight reached a steady state. While dry, it was weighed and measured. The bulk density could then be computed to a precision of  $\frac{1}{4}$  percent. The main source of error was uncertainty in the sample volume caused by chipping of edges while sawing the rock.

#### COMPOSITION

The composition of Arkansas Novaculite was determined by X-ray diffraction. Optical examinations of thin sections were made of all rocks and fabric studies were made on all but the Sioux quartzite and Arkansas Novaculite. Yale marble and Spargen limestone were both more than 99 percent calcite. Arkansas novaculite, Sioux quartzite, and Eureka quartzite each contained more than 99 percent quartz and Coconino sandstone contained about 97 percent quartz. The observed impurities in the last three rocks were mostly feldspars.

#### CRYSTAL DENSITY

A volumetric density-determination of the average crystal density was made using the rock with the highest percentage of impurities, Coconino sandstone. Crystal density agreed with that of quartz within the expected experimental error of  $\frac{1}{4}$  percent. Average crystal densities of the other rocks should also be equal to the densities of their major constituents with this precision.

#### POROSITY

Porosity of all rocks were computed by the formula

$$\text{Porosity (\%)} = 100 \frac{\rho_c - \rho_s}{\rho_c}$$

in which  $\rho_c$  is average crystal density and  $\rho_g$  is bulk density. Porosity of Coconino sandstone was also computed by comparing the weight of a water saturated sample of known volume with the weight of the same sample dried. The sample was saturated by evacuating air from its pores and submerging it in distilled water to which a wetting agent had been added. Then

$$\text{Porosity (\%)} = 100 \frac{W - D}{V}$$

when  $W$  is wet weight in g,  $D$  is dry weight in g, and  $V$  is volume in cc. Porosity determined by this method was 23 percent, slightly less than the 26 percent value determined for the same sample by the crystal density method. A slight disagreement in this direction is expected since the water does not completely fill all pores.

The porosity of Coconino sandstone samples from two blocks averaged 25 percent. Porosity of Indiana limestone averaged 12 percent. Porosity of all other rocks was less than 1 percent.

#### WATER ABSORPTION

Dried samples of all rocks were allowed to stand in a room in which the humidity varied from 40 to 60 percent. These samples were weighed to 0.1 percent precision at intervals during the two days after drying. None of the rock samples changed weight sufficiently to indicate an appreciable absorption of water from the atmosphere. It is concluded that water absorption from the atmosphere probably did not affect the dried rocks used in the shock wave experiments.

#### SOUND VELOCITY

Transducer measurements of sound velocity were made on samples of each rock and on many of the pieces used in shock experiments. The apparatus has two 1/2-inch-diameter piezoelectric transducers mounted in 1-inch-diameter steel pistons in a press which will exert up to a 2250-lb force on the sample. Birch<sup>13</sup> observed that a unidirectional stress on a rock sample produced nearly the same effect on sound velocity, in the direction of the stress, as an equal hydrostatic stress. Dried rock samples were measured at the highest applied stress they could withstand so that the value of sound velocity would be nearer the value of precursor

velocity in shock experiments. Birch found that values of sound velocity of a rock at atmospheric pressure varied widely when measurements were made on different samples of the rock. This was also found to be true in our measurements. Velocity rose rapidly in most rocks as the first hundred atmospheres on different samples of a rock gave small scatter in sound velocities.

#### SAMPLE PREPARATION

Specimens used in shock experiments were sawed with a rotary diamond saw. The surfaces of the quartzites and novaculite which would be observed or would be attached to backing plates or to explosive slabs were then lapped. All rocks were then heated at 120°C until they were dry, i.e., until weight reached a steady state. The surfaces of the Yule marble and the porous rocks were ground, while dry, after they were heated.

All specimens were measured and weighed. Values of bulk density could be calculated to 1% percent for large specimens. The same values were used for most of the small pellets which could not be measured within such small error.

#### CALCITE PREPARATION

The calcite specimens were cut from naturally occurring "Iceland spar" found in Chihuahua, Mexico. The pellets were usually about 1/4 inch thick and about 1 1/2 inch on a side. Only crystals that were colorless, free from cleavage, partings and obvious defects were used. Four different orientations were cut. The designation of a particular cut means that the shock wave travels parallel to the designated crystallographic axis (Fig. 33). The cuts used were X, Y, Z, and cleavage. Thus a Z-cut crystal will be orientated such that the Z-crystallographic axis is perpendicular to the surface of the backing plate and the ray of the shock wavefront will travel parallel to the Z-crystallographic axis. A similar designation is used for the X and Y crystallographic directions. The designation of cleavage cut is used to indicate that the ray path of the shock wave traveled parallel to the (0112) crystal plane.

The cleavage cut calcite was prepared by smoothing the proper faces of the calcite rhombohedron. The X, Y, and Z-cut calcite was prepared by orientating the rhombohedron by an analysis of the X-ray lattice pattern and cutting the proper thickness from the crystal. After the cuts were made

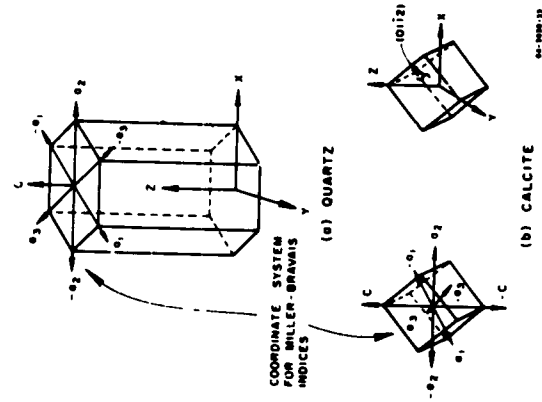


FIG. 33 COORDINATE SYSTEMS USED IN  
HEXAGONAL CRYSTALS

they were again checked by X-ray Laue patterns; and if necessary re finished until the orientation was within the proper tolerance.

#### TOLERANCES

The tolerances used in constructing the experiments are the following:

1. Crystal cuts within  $\pm 1$  degree
2. Pellet surfaces plane within  $\pm 0.0002$  inch
3. Backing plate within  $\pm 10$  minute of arc.

# APPENDIX C

## PROGRAM FOR TWO-DIMENSIONAL WEDGE EXPERIMENTS

Most of the experiments on this project used the wedge geometry and the optical lever arm recording method. Diagrams of experimental setups are shown in the previous section describing the experiments.

The detonation velocity is determined from a separate oscillographic record of the times at which the detonation front "connects" a series of electrical contacts.

The time and position coordinates of the wave-front arrival and position of the displaced trace are measured from the streak camera record. The measurements are made with a Vanguard Motion Analyzer, Model 74 W, which magnifies the 33 mm film approximately five times and contains screw-driven crosshairs for distance measurements. The over-all magnification is determined directly by measuring the image of a ruler included in the experimental setup.

Analysis of this data to derive equation of state points, using a desk calculator, might take several days, but the computer program described in this Appendix does it in a matter of minutes.

The basic equations for this analysis are the Rankine-Hugoniot relations, which relate normal stress  $\sigma$ , density  $\rho$ , and particle velocity ahead ( $u_0$ ) and behind ( $u$ ) a shock wave advancing at velocity  $U$ :

$$\sigma = \sigma_0 + 10\rho_0(U - u_0)(u - u_0) \quad (C-1)$$

$$\frac{\rho_0}{\rho} = \frac{(U - u)}{(U - u_0)}$$

(As written here, the units are mm/ $\mu$ sec or km/sec for velocity, g/cc for density, kilobars (kb) for stresses. Subscript "0" refers to variable ahead of the shock and no subscript refers to the variable behind shock.)

Since the state ahead of the shock may be presumed known, these two equations contain four unknown quantities,  $\sigma$ ,  $U$ ,  $u$ ,  $\rho$ , and if any two can be measured the other two may be calculated to give the state behind the shock. The optical lever arm recording method is designed to measure shock velocity  $U$  and particle velocity  $u$ .<sup>4</sup> Shock velocity is derived from the apparent velocity with which the break-out point of the shock front (discontinuities in traces, Fig. 12) moves across the film, i.e., from the slope of the dotted line in Fig. 12, and particle velocity from the distance the traces are displaced by the shock front.

In the balance of this Appendix the working equations for the analysis sketched above will be derived and the computer program which applies them will be described.

#### CURVE FITTING

To obtain the apparent velocity of the point of intersection of the shock front and wedge face from the record of Fig. 12, it is necessary to find the slope of a curve represented by a limited number of points (the dotted line). The merits of various schemes for accomplishing this are rather debatable and subject to a good deal of arbitrariness; some investigators sketch a line through the points with a French curve and approximate the tangent with a ruler, some prefer to use "smoothing formulas" such as those found in numerical analysis texts, which amount to replacing the experimental curve by short overlapping sections of polynomials, and some prefer to adjust the coefficients of various formulae to fit the data over a more-or-less wide range.

For this project the latter course was chosen, on the grounds of reproducibility, convenience, and adaptability to machine computation, and we fit (in the least squares sense) the shock arrival times  $t$  and positions  $x$  by a quadratic,  $t = c_1 + c_2 x + c_3 x^2$ . We chose to work with  $t$  a function of  $x$ , rather than vice-versa, because a single curved shock front can and sometimes does break through the surface at two different places at the same time but cannot break out at the same place at two different times; we chose a polynomial for simplicity and convenience, and a quadratic rather than a cubic because the cubic gave no noticeable improvement in most data (Fig. 34) and occasionally injected an inflection point amongst the data, leading to such unphysical results as calculated pressure increasing with greater distance from the explosive. The quadratic is

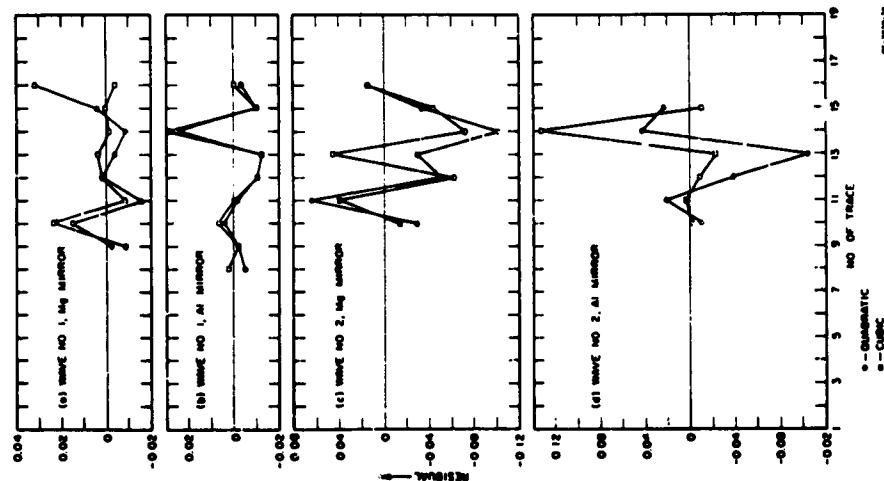


FIG. 34 PLOT OF RESIDUALS OF CUBIC AND QUADRATIC POLYNOMIALS

immune to this particular aberration, having no inflection point. The residuals of the fit are about the size of the errors to be expected in reading the film.

At first, there was a certain amount of worry from what seemed to be systematic bias in the curve fitting: frequently there would occur runs of as many as four or six consecutive points, out of perhaps twelve or sixteen, on the same side of the calculated curve. However, calculation shows that this is rather to be expected than not. For instance, the probability that four random errors will not all have the same sign is  $1 - (1/2)^3 = 7/8$ , but in a set of 10 points there are  $10 - 4 + 1 = 5$  sets of four consecutive points, so the probability that none of these sets will be uniformly of the same sign is  $(7/8)^5 = 16807/32768 = 51.3$  percent. The contrary probability, that there will be at least one run of four or more consecutive signs, is thus 48.7 percent. Fig. 35 compares the results of such calculations, assuming a total of 10 points in all cases, with the actually observed frequencies. There seem at first to be rather too many runs of six but this is because several shots had 16 or so points per wave. The striking lack of 5 point-long sequences is unexplained but not believed significant.

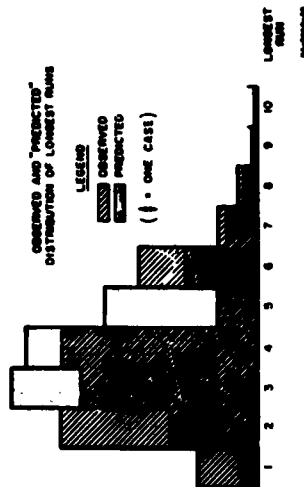


FIG. 35 OBSERVED AND PREDICTED DISTRIBUTION OF LONGEST RUNS

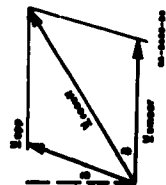


FIG. 36 SKEAR RECORD VELOCITY DIAGRAM

## APPARENT VELOCITY

Fig. 36 shows how the motion of the breakout point along the wedge face ( $U_{app}$ ) and of the image of the wedge face along the film ( $U_{mirror}$ ) combine to give a resulting motion ( $U_{result}$ ) which corresponds to the tangent of the dotted line in Fig. 12. These two component motions are nominally at right angles, but actually the slit is usually tilted by a small angle  $\delta$  ( $\sim 0.5$  deg), which can be measured from an image of the stationary slit exposed on the same film before the mirror of the smear camera begins to rotate.

Taking components parallel and perpendicular to  $U_{mirror}$ ,

$$U_{result} \sin \phi = U_{app} \cos \delta$$

$$U_{result} \cos \phi = U_{mirror} + U_{app} \sin \delta$$

from which

$$U_{app} = \frac{U_{mirror}}{\cot \phi \cos \delta - \sin \delta} \quad (C-2)$$

The parameter  $U_{mirror}$  is evaluated from

$$U_{mirror} = \frac{\text{screen inches/microsecond} \times \text{object inches/screen inches}}{\text{a millimeter/inch}} \quad (C-3)$$

and  $\cot \phi$  from the polynomial fit,  $t = c_1 + c_2 x + c_3 x^2$ , i.e.,

$$\cot \phi = \frac{dt}{dx} = c_2 + 2c_3 x' \quad (C-4)$$

evaluated at the position of the displaced image,  $x'$ .

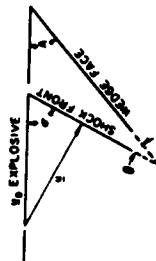
# SHOCK VELOCITY

From Fig. 37(a),

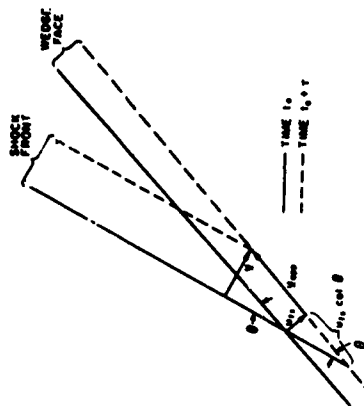
$$\begin{aligned} U &= U_g \sin \alpha \\ \theta &= \alpha - A \end{aligned} \quad (C-5)$$

where  $U_g$  is the detonation velocity of the explosive. Figure 37(b) shows the shock front and wedge face at two successive instants, for the general case in which the wedge face has been set in motion by a preceding shock front. From this diagram,

$$\frac{U}{U_{app} + u_{f, \cot \theta}} = \sin \theta$$



(a)



(b)

FIG. 37 SHOCK VELOCITY GEOMETRY

Combining this with Eqs (C-5),

$$\theta = \arctan \frac{u_{f,} - U_{app} \tan A}{\frac{U_g}{\cos A} + u_{f,} \tan A - U_{app}} \quad (C-6)$$

The wedge angle  $A$  is measured before the shot is fired.  $U_g$  is found from the time between electric contact of pairs of "pin" switches on the explosive slab.  $U_{app}$  is calculated as indicated in the preceding section, and  $u_{f,}$  as in the next. Equations (C-5) and (C-6) are then used to calculate the shock angle  $\theta$  and shock velocity  $U$ .

## PARTICLE VELOCITY

When a shock wave across which the particle velocity change is  $\Delta u (= u - u_0)$  is incident on a free surface at an angle  $\theta$ , it imparts to the free surface a velocity  $\Delta u_{f,} (= u_{f,} - u_{f,0})$ . Referring to Fig. 38(a),  $\Delta u_{f,}$  is the vector sum of the changes in particle velocity across the incident, and reflected shocks,  $\Delta u$  and  $\Delta u_r$ . By the free-surface approximation these are equal,  $\Delta u = \Delta u_r$ . Thus  $\Delta u_{f,} = 2\Delta u \cos \epsilon$ . But  $2(90^\circ - \theta) = 2\epsilon + \beta = 180^\circ$ , so  $\epsilon = \theta - \beta/2$  and  $2 \cos \epsilon = 2 \cos (\theta - \beta/2) = 2 \cos \theta \sin \beta/2 + 2 \sin \theta \sin \beta/2 = 2 \cos \theta + \beta \sin \theta$ , if  $\beta$  is small. Thus we get

$$\Delta u_{f,} = \frac{\Delta u_{f,}}{2 \cos \theta + \beta \sin \theta} \quad (C-7)$$

The change in free-surface velocity is calculated from the angle through which the wedge face is turned, which in turn is calculated from the displacement of the light source image, as follows [Fig. 38(a), (b), Fig. 12]

$$\begin{aligned} \Delta u_{f,} &= U_{app} \tan \beta \\ \tan \beta &= \frac{y}{2d} \end{aligned} \quad (C-8)$$

$$y = \frac{x' - x}{f_L}$$



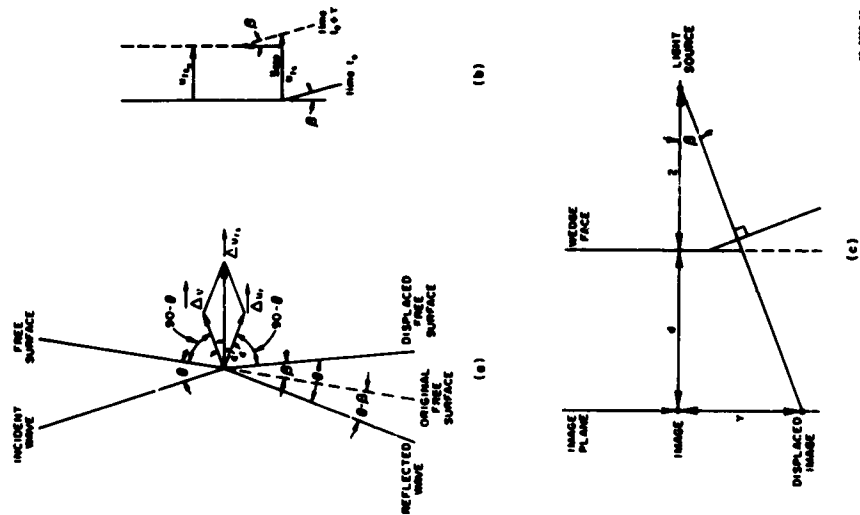


FIG. 38 PARTICLE VELOCITY GEOMETRY

where  $I_L$  is the magnification factor from light source to Vanguard screen,  $I_L = \text{screen distance true distance}$ .

#### IMPEDANCE MATCH

If the method is to yield pressure data, the optical lever are recording technique requires that the surface of the specimen remain a good reflector after the shock wave hits it. The rocks studied in this project do not meet this requirement, even with the best obtainable polish and a vacuum-deposited metallic reflecting surface. This problem was solved by attaching to the rock surface a 0.5-mm-thick strip of aluminum or magnesium with a highly polished outer surface. Then a shock wave which produces a change in the dynamic state of the rock shown on W of Fig. 39, for example, strikes the interface, a shock is refracted into the mirror and another is reflected back into the rock. If the mirror does not fly off the surface, continuity at the interface requires that both refracted and reflected shocks reach the same terminal point  $C$ , which

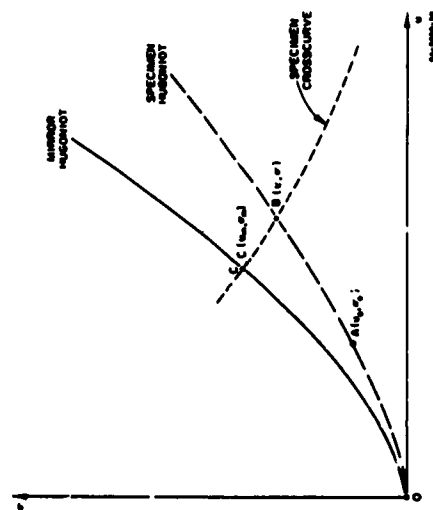


FIG. 39 IMPEDANCE MATCH DIAGRAM

therefore lies at the intersection of the mirror Hugoniot and the specimen cross curve (locus of states attainable by reflected waves) through state B. The final shock OC then propagates to the mirror surface, where it causes deflection of the light-source images and hence can be observed and calculated as outlined above.

(If the rock Hugoniot lies above the mirror Hugoniot, HK will be a rarefaction instead of a shock but the computations are the same.)

The state in the specimen behind the incident shock, H, could therefore be calculated as the intersection of the specimen's Hugoniot through A and its cross curve through C, if the latter two curves were already known. In other words we can calculate the Hugoniot of the rock if we know its Hugoniot and cross curve—but the cross curve is (for nonporous materials) the reflection of the Hugoniot about point B and the section AB of the Hugoniot can be approximated as a straight line whose slope is given by the jump condition,  $\sigma = \sigma_0 + 10\rho_0(U - u_0)(u - u_0)$ . State B is thus found by the intersection of this equation with  $\sigma = \sigma_0 - 10\rho_0(U - u_0)(u - u_0)$ , i.e., by

$$u = \frac{1}{2} \left( u_0 + u_0 + \frac{\sigma_0 - \sigma_0}{H} \right) \quad (C-9)$$

$$\sigma = \frac{1}{2} [\sigma_0 - \sigma_0 - H(u_0 - u_0)]$$

where

$$H = 10\rho_0(U - u_0)$$

$U$  and  $u_0$  are the shock velocity in the specimen and particle velocity of the mirror, respectively, calculated from the film record as outlined in preceding sections, with a small correction to the angle  $\theta$  between shock front and mirror surface to account for the change in direction of the shock at the specimen-mirror interface. Across the interface Snell's law applies

$$\frac{\sin \theta_0}{U_0} = \frac{\sin \theta}{U}$$

with  $\theta_0$  and  $U_0$  the shock angle and velocity in the mirror. Since  $\sigma_0 = 10\rho_0 U_0 u_0$ , this may be written

$$\cos \theta_0 = \sqrt{1 - \left( \frac{\sigma_0 \sin \theta}{10\rho_0 U_0 u_0} \right)^2} \quad (C-10)$$

The pressure in the mirror,  $\sigma_0$ , is obtained from  $u_0$  by means of the (known) Moraghan equation of state of the mirror material,

$$\sigma_0 = A_0 \left( (\rho_0/\rho_0)^{\gamma} - 1 \right)$$

where  $A_0$  and  $\gamma$  are known constants. Combining this with Eqs. (C-1) for the mirror material gives

$$\sigma_0 \left[ 1 - \left( 1 + \frac{\sigma_0}{A_0} \right)^{-1/\gamma} \right] - 10\rho_0 u_0^2 = 0 \quad (C-11)$$

which must be solved for  $\sigma_0$ . This is done by the method of binary chopping, in which an interval in which the root is known to lie is successively halved until the root is located to three decimal places.

The over-all scheme of the impedance-match calculations, to sum up, is as follows: Shock velocity  $U$  is found from Eqs. (C-5) and (C-6) (this is the velocity appropriate to the specimen rather than the mirror since the travel time through the mirror is only a small fraction of the total travel time), particle velocity  $u$  calculated from Eqs. (C-7) and (C-8) is taken as a first approximation to  $u_0$  (not exact because  $\theta$  needs to be corrected for refraction) and an approximate  $\sigma_0$  found from Eq. (C-11). These approximations are improved by use of Eqs. (C-10), (C-7), and (C-11) (the improvement could be iterated but the first cycle change is already small), and the state in the specimen behind the incident shock is calculated from Eq. (C-9).

#### MULTIPLE-SHOCK RECORDS

The analysis of the preceding section drastically oversimplifies the interactions arising when a multiple-shock system is incident on the rock-mirror interface. It is the purpose of this section to develop more fully the details of the interaction and to show that the simplification is

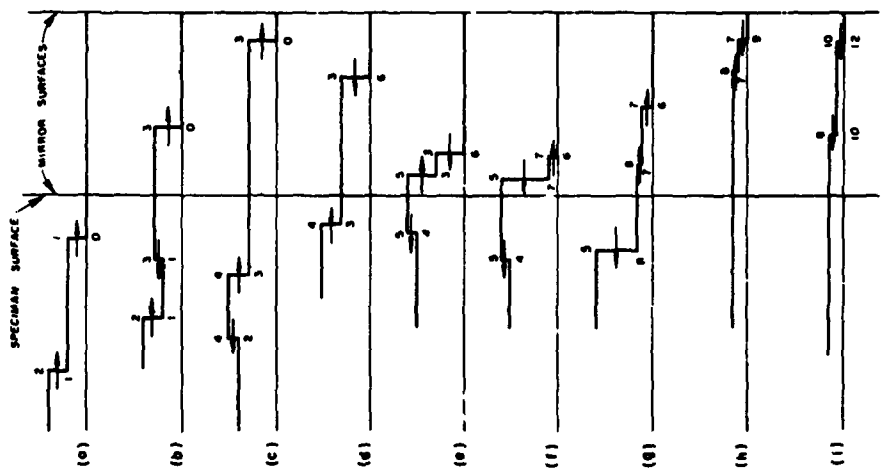


FIG. 40 STRESS PROFILE AT SELECTED TIMES  $\Delta t < 7$

justified, subject to an easily tested relation among the time delay between the waves, the mirror thickness, and the sound speed in the mirror.

Figure 40(a) shows a two-wave system 0-1, 1-2, propagating through the rock toward the mirror. When the first wave, 0-1, strikes the interface it is reflected as 1-3 and refracted as 0-3 (Fig. 40(b)). The stress-particle-velocity point behind shock 1-3 must lie on the reflected rock Hugoniot through point 1 (Fig. 41) and the state behind 0-3 must lie on the mirror Hugoniot through point 0; since these are the same state (required by continuity) the stress-velocity point is at the intersection of the curves, point 3 in Fig. 41. In Fig. 40(c), shocks 1-3 and 1-2 have collided and interpenetrated (or reflected from each other) to produce 3-4 and 2-4. By the same reasoning as above, state 4 in Fig. 41 lies at the intersection of the rock Hugoniot through 3 and the reflected rock Hugoniot through 2. Next the shock 0-3 is reflected from the free surface as a rarefaction 6-3 (Fig. 40(d)). The velocity indicated for point 6 in Fig. 41 is observed as a free-surface velocity and one calculates back successively to points 2 and 1 as indicated in Fig. 41. At time E, (Fig. 40(e)) wave 3-4 passes into the mirror, producing 3-5 and 4-5. Next 3-5 and 3-6 interact in the mirror to produce 5-7 and 6-7 (Fig. 40(f)). 5-7 is reflected and refracted to form 7-8 and 5-8 (Fig. 40(g)). and 6-7 reflects from the free surface as 7-9 (Fig. 40(h)). State 9 is observed at the mirror surface and calculations proceed to states 5 and 2. Shocks 7-8 and 7-9 continue to bounce back and forth in the mirror, crossing and recrossing to produce states 10, 11, 12, etc. Figure 42 shows the full system of shock waves in the time-position coordinate plane.

Figures 40, 41, 42 are drawn for the case where the time separation between the original shocks,  $\Delta t$ , is less than the "reverberation time," or time for a shock to travel across the mirror and back. The important point is this: although material in the rock near the rock-mirror interface follows the path 0-1-3-4-5-8, material in the mirror near the interface follows 0-3-5-7-8, and material in the mirror near the free surface follows 0-3-6-7-9, the final observed result (states 6, 9, 12, etc.) is the same as if material in the rock had followed 0-1-2 while that in the mirror followed 0-3-6 and 0-5-9, and these latter paths are those assumed in the preceding derivation of the working equations for impedance-match calculations.

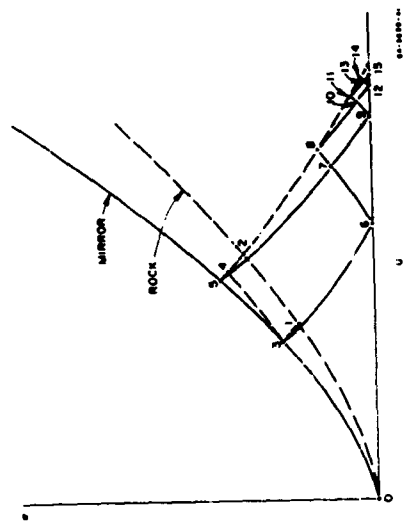


FIG. 41 STRESS-PARTICLE VELOCITY DIAGRAM,  $\Delta T < \tau$   
(See Figs. 39 and 40)

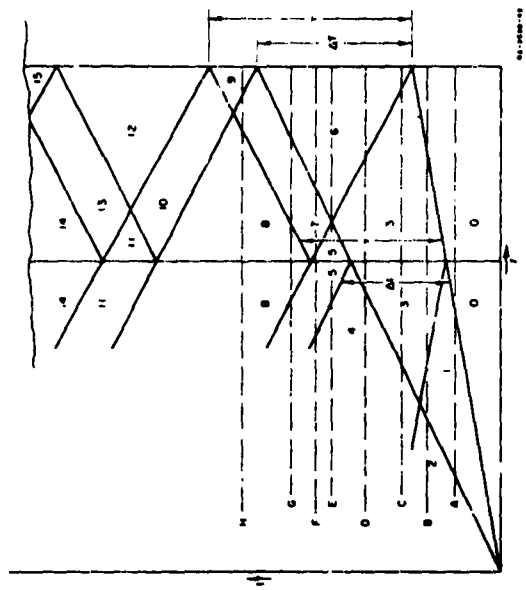


FIG. 42 TIME POSITION DIAGRAM,  $\Delta T < \tau$

On the other hand, if the separation of the incoming waves is greater than the reverberation time,  $\Delta T > \tau$ , this simplification does not apply. Figures 43, 44, 45 drawn for the same set of incident waves as Figs. 40, 41, 42 but a mirror about one-half as thick, show how the reverberation from the first wave arrives at the mirror-rock interface before the incident second shock [compare Fig. 43(c), (d), (e) to Fig. 40(c), (d), (e)], so that analysis according to the above simplified point of view (dotted lines, Fig. 44) would lead to erroneous results. Theoretically state 2 could still be located (for instance, by constructing points 7' and 8' and extrapolating) but in practice it is difficult if not impossible to tell (after the first reverberation) whether a given set of wiggles in the traces on the film represents the arrival of a genuine second (or third) wave, so anything beyond the reverberation time is simply ignored in reading the film.

If the incident shock system contains three waves the interactions are more complicated but the result is the same: any wave that arrives at the mirror surface earlier than the reverberation time of the first shock is analysed from the simplified point of view to give the correct state behind the original wave, anything that arrives later than one reverberation time ( $\approx$  twice mirror thickness divided by sound speed in mirror behind first shock) after the first shock is ignored.

The following three sections present respectively a key to the symbols, a flow chart, Fig. 46, and a listing of the ALGOL program for the Burroughs 220 computer which embodies the preceding analysis.

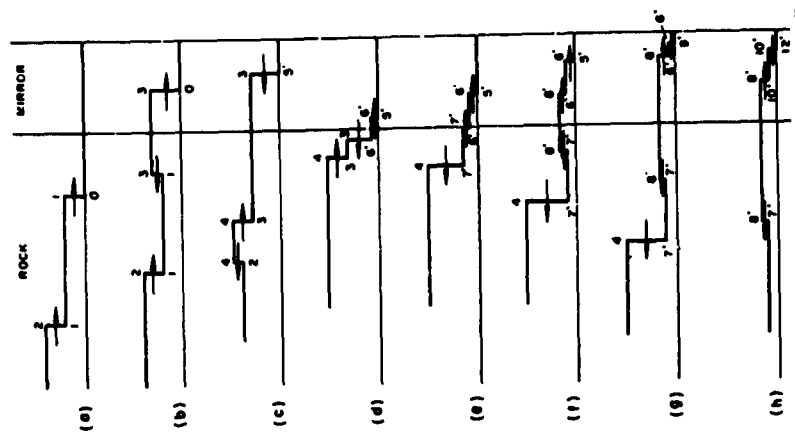


FIG. 43 STRESS PROFILES AT SELECTED TIMES,  $\Delta T > \tau$

# KEY TO SYMBOLS

$SOFT(X) = \sqrt{1 - X^2}$  (double-precision arithmetic)  
 $PUS(N) = 1$  if program control switch N is ON  
 $PUS(N) = 0$  if program control switch N is OFF

PALS - curve-fitting routine    UNSEL - equation-solving routine

Principal variables				NAME IN PROGRAM		LINE NO. (Where Calculated)	
NAME IN TEST	EQ. NO. (Where Derived)	QUANTITY		SIGMA		81B, 83C	
$\sigma$	1, 2	Normal stress behind shock wave		RATIO		84	
$\rho_0, \rho$	1	Density ratio across shock		UA		69G	
$U_{app}$	2	Apparent velocity		K		52	
$U_{camer}$	3	Camera film-viewer parameter		SUM		69E & F	
$\cos \delta$	4	Slope of first-arrival line		US		71	
$\theta$	5	Shock velocity		THETA		70C	
$\phi$	5	Angle between shock and wedge face		ALPHA		70A & B	
$\alpha$	6	Angle between shock and explosive		IMP		76A, 88G, 81C	
$\Delta u$	7	Increase in particle velocity across shock		IMFS		76A	
$\Delta U_{fs}$	8	Increase in free-surface velocity		BETA		75A	
$\beta$	8	Turning angle of wedge face		UP		81A, 83B	
$\gamma$	8	Shift in image position		H		76A & B	
$\alpha$	9	Particle velocity behind shock		SIN THETA COS THETA		80F & F	
$H$	9	$10\rho_0(U - \rho_0)$		G(P)		16-17	
$\sin \phi_0$	10	sine cosine $\theta$ after refraction					
$\cos \phi_0$	11	Equation to be solved for $\phi_0$					

Frequency constants, etc.				DI. RATE		AVE. T1, T2	
NAME LINE NO. (Where Calculated)	TENNO	SD, CD, DR	AN	TENNM		51	52, 72BSC, 74A, 81B-D, 90A & B
	47	48	49	50			
	DENRM, RMS	TANA	DEPTH				
	63D-G, 64A-D	69D	72A				

Loop indices				J		J	
NAME	J1	J2					
CONTROLS	54-90H	68-89					

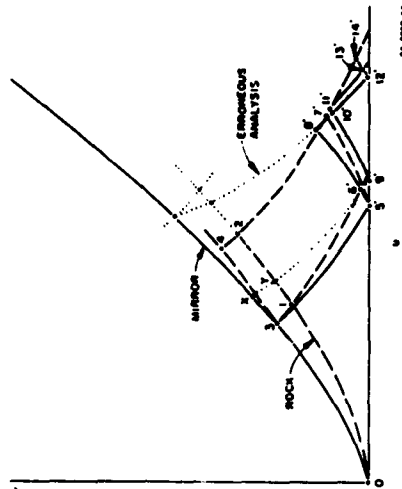


FIG. 44 STRESS-PARTICLE VELOCITY DIAGRAM,  $\Delta T > \tau$   
(See Figs. 42 and 43)

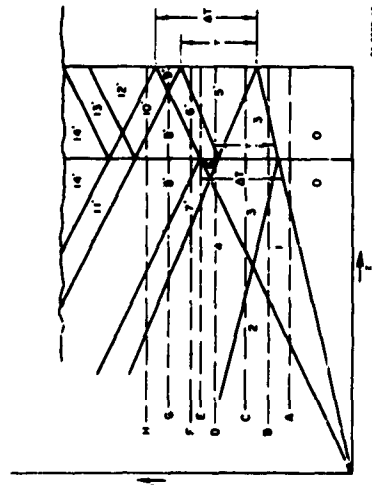


FIG. 45 TIME POSITION DIAGRAM,  $\Delta T > \tau$



[illegible]



PROCEDURE BISEC (X0,X1,EPP,EPS,YS,F111S)

BEGIN

COMMENT: BISECTION ROUTINE TO FIND ROOTS OF ANY EQUATION Y=FIXIS

Y0 = YFIXIS

F1 = F111S

IF ABS(F0) LEQ EPS

Y=EOS RETURNIS

Y=EOS RETURNIS

Y=EOS RETURNIS

Y=EOS RETURNIS

Y=EOS RETURNIS

Y=EOS RETURNIS

Y=EOS RETURNIS

Y=EOS RETURNIS

Y=EOS RETURNIS

Y=EOS RETURNIS

Y=EOS RETURNIS

Y=EOS RETURNIS

Y=EOS RETURNIS

Y=EOS RETURNIS

Y=EOS RETURNIS

Y=EOS RETURNIS

Y=EOS RETURNIS

Y=EOS RETURNIS

Y=EOS RETURNIS

Y=EOS RETURNIS

Y=EOS RETURNIS

Y=EOS RETURNIS

Y=EOS RETURNIS

Y=EOS RETURNIS

Y=EOS RETURNIS

Y=EOS RETURNIS

Y=EOS RETURNIS

Y=EOS RETURNIS

Y=EOS RETURNIS

Y=EOS RETURNIS

Y=EOS RETURNIS

Y=EOS RETURNIS

Y=EOS RETURNIS

Y=EOS RETURNIS

Y=EOS RETURNIS

OTHER=1525

GO TO ROOTS

ENDS

ROOTS=X0,X1,X2

ENDS

ROOTS=X0,X1,X2

ENDS

ROOTS=X0,X1,X2

ENDS

ROOTS=X0,X1,X2

ENDS

ROOTS=X0,X1,X2

ENDS

ROOTS=X0,X1,X2

ENDS

ROOTS=X0,X1,X2

ENDS

ROOTS=X0,X1,X2

ENDS

ROOTS=X0,X1,X2

ENDS

ROOTS=X0,X1,X2

ENDS

ROOTS=X0,X1,X2

ENDS

ROOTS=X0,X1,X2

ENDS

ROOTS=X0,X1,X2

ENDS

ROOTS=X0,X1,X2

ENDS

ROOTS=X0,X1,X2

ENDS

ROOTS=X0,X1,X2

ENDS

ROOTS=X0,X1,X2

ENDS

ROOTS=X0,X1,X2

ENDS

ROOTS=X0,X1,X2

ENDS







## RELATIONSHIPS OF ROCK PARAMETERS

## APPENDIX D

## RELATIONSHIPS OF ROCK PARAMETERS

Shock wave data from polycrystalline rocks differ from data on single crystals. These differences are the change in peak stress of the first wave and the change in the locus of stress-particle velocity states. This occurs in a pressure range of a few kilobars to about one hundred kilobars.

Differences in shock data are correlated with differences in the composition and texture of the rock.

## COMPOSITION AND TEXTURE IN SEDIMENTARY ROCKS

The basis by which the igneous rocks are classified is much different from the basis used in classifying metamorphic rocks. And likewise, the basis for classifying sedimentary rocks is still different. This is made more complicated by the fact that many geologists use variations of the various classifications if it suits their needs. However, the parameters that are used in most all of the classifications are composition and texture. These same parameters control shock wave propagation in rocks. It might be wise to discuss these parameters from both points of view.

Krynine<sup>11</sup> states, "there are altogether ninety-three important derived properties of parameters of sedimentary rocks, but most of these are quite unnecessary for purposes of megascopic identification." Thus, theoretically there are ninety-three different features which can be assigned to the various parameters of a sedimentary classification. However, Pettijohn<sup>12</sup> states, "It is not possible to construct a classification based on all known or knowable properties. A workable classification will take into account two or three and ignore all others. Each choice requires that the (defining) properties be not only genetically significant but that they be the most significant."

The parameters that seem to be most significant are those of composition and texture. Most all of the observations and inferences about a rock can be grouped under composition and texture. Thus, these parameters

are perhaps used more than any other two parameters in the classification of a sedimentary rock.

Many genetic features can be inter-related in terms of composition and texture. The parent rock will control the composition of the detrital grains.

The rate of erosion will control the rate of deposition, thus affecting the texture of the sedimentary rock. During transport of detritus to the deposition site, the shape, size, and roundness of grains will be changed. The effect of density, shape, size, and roundness on sorting grains will be multiplied by the additional sorting from hydraulic features of viscosity, turbulence, fluid velocity during the time of deposition. Features such as the depth of water at the deposition site, temperature, salinity, acidity, oxidation-reduction potential, and its position with respect to the deposition interface, freedom of circulation, muddiness of water, and the nature of organic life all affect the texture of the sediment that is being deposited. Even after deposition, composition and texture are affected by diagenetic changes that take place in the sediment.

Composition and texture in sedimentary rocks is genetically significant but different measures of composition and texture are necessary in a chemical rock in comparison to a clastic rock. For example, application of the Udden-Wentworth grade scale to a clastic rock has genetic meaning but application of this scale to a precipitated rock does not. Instead, textures and grade sizes of chemical rocks, such as igneous textures and grade sizes, must be applied if there is to be any genetic interpretation. The application of the Udden-Wentworth grade scale to rocks that have been diagenetically changed or that have both clastic and chemical constituents has little genetic meaning. But neither will it be valid to apply the chemical rock texture and grain size to these "hybrids." Instead a combination of the two methods must be used to gain genetic meaning.

Duppley, Krumbein, and Slone<sup>10</sup> give four different constituents of which all sediments are composed. These are:

- "1. Detrital particles which have been carried to the site of deposition and under the prevailing energy state of the transporting medium settle downward to the depositional interface
2. Inorganic salt precipitates from solution at or above the depositional interface and is incorporated as an integral part

3. Inorganic salts precipitated on the existing grains or crystals, or in the interstitial spaces
4. Material produced by organic activity."

Many sedimentary rocks are either endogenetic or exogenetic. That is, exogenetic grains are the clastic grains that are carried to the deposition site whereas endogenetic material is formed at the site of deposition. Extreme examples of endogenetic and exogenetic rocks are a chemically precipitated limestone and a well sorted sandstone, respectively.

Most sedimentary rocks are composed of mixtures of the endogenetic and exogenetic constituents, and thus show varying characteristics of each. These are termed "hybrid" by Pettijohn.<sup>11</sup> Superimposed on the textures due to mechanical and chemical sedimentation and commonly obscuring them may be those textures induced by recrystallization and replacement (diagenesis).<sup>12</sup>

In trying to systematically describe the composition and textures of sedimentary rocks, many classifications have been constructed. The sandstones have been the first and easiest to classify. Texture and composition will indicate the maturity of the clastic rock as well as the source area. Composition and texture will also indicate the nature of the transporting medium before burial. Maturity, source, and transporting medium are three of the most important genetic interpretations that can be made in rock analysis.

Pettijohn<sup>11</sup> used the three parameters of maturity, source, and "fluidity index" as the basis of sandstone classification. The source rock parameter is measured by the ratio of feldspar to other rock fragments. The maturity index is measured by the ratio of feldspar to quartz fragments. And "fluidity index" is measured by the ratio of detrital grains to matrix.

From the three parameters of sandstone classification four groups of clastics can be derived: graywackes, lithic sandstones, arkosic sandstones, and orthoquartzites. These groups are indicative of different tectonic environments and give maximum possible information about the genesis of the sandstone that can be obtained.

Other clastic sedimentary rocks such as purely clastic limestones and conglomerates can also be described in terms of maturity and fluidity factor (and also source area in the case of conglomerate). Composition and texture will be the method of indicating these parameters.

Two types of porosity in sedimentary rocks are possible. Both may exist in the rock to some degree of importance but they will be discussed separately. Two types of porosity may be termed primary porosity and secondary porosity.

Primary porosity is a characteristic of the rock that is determined at the time when the sediment is deposited. A quartz sandstone with no cement would be a typical example. But in general, pore space in a sediment may be reduced either by filling pores with a cement or by compacting the sediment to a more lithified state. Compaction is most important in consolidating muds and clays and not so for sand-sized particles.

The primary porosity of any clastic rock is a combination of the following parameters: packing, sorting, particle shape, particle size, cement, compaction.

If the clastic rock were composed of only spheres of a uniform size, the porosity would be 47.6 percent if the spheres were cubically packed and 25.9 percent if the spheres were rhombohedrally packed. The size of the grains is unimportant. From this, it follows that the porosity may range between the two values if packing is not completely uniform. If the sorting of grains is good, i.e., grains are the same size, porosity will range between the above two values depending upon the packing. If sorting is poor, porosity may be much less than the above values because smaller grains will fill the spaces between larger grains. The particle shape can influence porosity because deviation in shape from a sphere will distort the packing and thereby affect porosity. Grain size is usually not significant in changing porosity but it may greatly affect it if the grains are very small. A small grain size usually means that the grain is very irregular in shape and thereby causes a very irregular packing. Some muds have a pore space of 60 to 90 percent, and diatomaceous earths can easily have porosities of 75 percent. Cement can reduce porosity as can compaction.

Compaction effects, if primarily controlled by grain size, can be separated into compaction of unconsolidated sediments and compaction of lithified sediments. Compaction of unconsolidated sediments is not of interest to us but it consists mainly of pore reduction and squeezing fluids out of the sediment. Sandstones are generally only compacted about 10 percent or so but muds are compacted up to 30 or 40 percent.

Chemical sediments cannot be indicative of maturity and transporting medium since their composition and texture was formed *in situ*. Instead, a chemical sediment will have its composition and texture interpreted in terms of salinity, acidity, redox potential and other chemical properties of the precipitating medium and later diagenetic changes.

The argillaceous sediments contain chemical, biochemical, and clastic elements. These sediments are a hybrid class having characteristics of both chemical and clastic sediments. Moreover, the clay particles included in the clastic element are also affected by chemical changes. Pettijohn states, "A satisfactory classification, yet to be worked out, must contain elements of both classifications" (chemical and clastic).

Some writers have tried to group clastic, chemical and argillaceous rocks into different suites that indicate tectonic environment. These suites are basically the graywacke, arkose, and orthoquartzite group of sandstones but expanded to include chemical and argillaceous rocks. The concept of suites should be useful but since sandstones have been the only group that has been successfully classified into suites, other chemical and argillaceous rocks will have to be grouped into suites before the concept becomes completely useful.

#### EFFECT OF COMPOSITION AND TEXTURE ON SHOCK DATA

Thus, we see that composition and texture of a rock is interpreted by the geologist to obtain information about the source of the rocks, its history and environment as it was being transported and effects during and following deposition. These same parameters of composition and texture determine the shock wave data for each rock.

**Composition:** Composition is the most important. Composition determines the velocity of the shock wave including flow, phase changes, and velocity of the elastic precursor. The over-all features of shock propagation are characteristic for each composition.

**Texture:** The shock effect of texture, i.e., grain size, shape, sorting, cement, etc., produce variations on the shock effect from composition. The effect from texture can be quite strong on some of the data. Thus, for the parameter of texture can be primarily considered in terms of porosity. Porosity is dependent upon many textural features, and it is necessary to determine which are most important.

Compaction of lithified sediments consists mainly of squeezing finer grained material into pores or in deforming grains plastically. A general rule is that larger grains are less easily compressed. Compaction in sandstones is quite often typified by an increase in the point contacts between grains.

"Some of the diagenetic processes in carbonate rocks continue after the rock has become lithified, and these contribute to secondary porosity. Compaction, cementation, solution, recrystallization, and dolomitization are all common in diagenetic as well as post-diagenetic changes. The porosity that results from these processes, when it can be determined, may be said to be secondary, whereas that which merely modifies primary depositional characteristics may be said to be primary."<sup>9</sup>

#### RELATION OF ROCKS STUDIED TO COMPOSITION AND TEXTURE

The rocks, as much as is possible, are selected because they have the fewest parameters to consider.

The sandstones and quartzites are composed of pure quartz grains. Little or no matrix is present. The grains are well sorted, rounded, and large enough so that the original porosities should lie between 47 to 26 percent. Cement is present. The preferred orientation of grains is small. From the parameters controlling porosity (packing, sorting, particle size, particle shape, cement, compaction), the only ones pertinent are original packing and cement. It might be that other parameters affect some of the shock properties, such as grain size, but these have not been noticed.

The marble and limestone are not as simple. The marble has been recrystallized and the porosity is secondary. The limestone had a higher original porosity but there has been cementation and some solution. The marble has a high degree of preferred alignment of grains. The parameters affecting shock properties are porosity, and mineral alignment. Again grain size may affect rise times of shock waves but it is not certain at this time. Parameters related to porosity are uncertain.

#### REFERENCES

1. Rice, M. H., J. M. Walsh, and R. G. McQueen, "Compression of Solids by Strong Shock Waves," *Solid State Physics*, ed by F. Seitz and D. Turnbull, Acad Press, Inc., 6, New York (1959).
2. Walsh, J. M., M. H. Rice, and R. G. McQueen, "Shock Wave Compression of 27 Metals - Equations of State of Metals," *Phys Rev* 108, 196.
3. Fieseler, G. R., "The Development of an Explosive Electric Transducer, Part I, Equation of State of Quartz," *Final Report on P.O. No. 18-1966-A for Sandia Corp., Livermore, California*, (1961).
4. Fieseler, G. R., "Shock Wave Compression of Hardened and Annealed 2024 Aluminum," *Jour App Phys* 32, 6, 1675-1687 (1961).
5. Katz, S., D. G. Thurn, and D. R. Garren, "Hugoniot Equation of State of Aluminum and Steel," *ibid*, 32, 4, 1413-1421, (1961).
6. Fieseler, G. R., "Shock Wave Compression of Quartz," *Puolter Laboratories Tech Report* 083-61, October 26, 1961.
7. Scherle, Jerry, "Shock Wave Compression of Quartz," *Jour of App Phys* 33, 3, 922-937, March 1962.
8. Ashworth, G. A., D. R. Bishler, A. R. Drenin, "A Study of the Volumetric Compressibility of Marble at High Pressures," *Bull Acad Sci USSR (Geophysics)*, 5, 463-466, May 1961.
9. Turner, F. J., D. T. Griggs, and H. Heard, "Experimental Deformation of Calcite Crystals," *Bull Geol Soc of Amer*, 65, 983-994, (1954).
10. Griggs, D., and J. F. Van der, ed., "Rock Deformation," *Geol Soc of Amer, Memoir* 79, March 1, 1960.
11. Felt, R., and C. E. Weaver, "A Study of the Texture and Composition of Quartz," *Amer Jour of Sci*, 250, 494-510, July 1952.
12. Moore, H. J., "Personal Communication," *Geologist*, U.S.G.S., Menlo Park, California, December 1961.
13. Williams, H., F. J. Turner, and C. M. Gilbert, "Petrography," W. H. Freeman and Company, San Francisco, (1955).
14. Pettijohn, F. J., "Sedimentary Rocks, sec ed Harper & Brothers, New York, (1953).
15. Birch, F., "The Velocity of Compressional Waves in Rocks to 10 Kilobars, Part 1," *Jour of Geoph Res* 65, 1083-1102, (1960).
16. Birch, F., "The Velocity of Compressional Waves in Rocks to 10 Kilobars, Part 2," *Jour of Geoph Res* 66, 2199-2224, July 1961.
17. Pettijohn, F. J., R. R. Schreck, and Rynise, "Symposium on Classification of Sedimentary Rocks," *Jour of Geol*, 56, (1948).
18. Dupless, E. C., R. G. Krumboltz, and L. L. Sloan, "The Organization of Sedimentary Rocks," *Jour of Sed Pet*, 20, 3-20, (1950).
19. Aldy, L. F., "Compaction and its Effect in Local Structures, Symposium," *Problems of Petroleum Geology*, A.A.P.G., (1954).
20. Levenstam, A. L., "Geology of Petroleum," W. H. Freeman and Co., San Francisco, (1956).
21. Meria, C. M., "Porosity, Permeability, Compaction (Foreword), Symposium, Problems of Petroleum Geology," A.A.P.G., (1954).



STANFORD  
RESEARCH  
INSTITUTE

MENLO PARK  
CALIFORNIA

#### Regional Offices and Laboratories

Southern California Laboratories  
2750 Wilshire Blvd.  
South Pasadena, California

Washington Office  
800 17th Street, N.W.  
Washington, D.C.

New York Office  
270 Park Avenue, Room 1710  
New York 17, New York

Detroit Office  
1750 Ford Building  
100 East Michigan  
Birmingham, Michigan

European Office  
P.O. Box 37  
Zürich 1, Switzerland

#### Representatives

Honolulu, Hawaii  
Foster Federal Building  
100 South King Street  
Honolulu, Hawaii

London, Ontario, Canada  
25 Spadina Park  
London W. 1, Ontario, Canada

London, England  
15 Abchurch Lane  
London W. 1, England

Milano, Italy  
Via Montebello 10  
Milano, Italy

Tokyo, Japan  
111 First Building  
1-1-1, Yamanote  
Tokyo, Japan

END